Thin–Walled Structures 200 (2024) 111920

Contents lists available at ScienceDirect

Thin-Walled Structures

journal homepage: www.elsevier.com/locate/tws

Full length article

Experiments and design of a kirigami-based multi-stage energy absorption structure subjected to axial impact

Baofeng Ruan [a,b], Lele Zhang [a,b], Weiyuan Dou [a,b,*], Ding Zhang [a], Sebastian Stichel [c]

[a] School of Mechanical, Electronic and Control Engineering, Beijing Jiaotong University, Beijing 100044, PR China
[b] National International Science and Technology Cooperation Base on Railway Vehicle Operation Engineering of Beijing Jiaotong University, Beijing 100044, PR China
[c] KTH Royal Institute of Technology, Department of Engineering Mechanics, Teknikringen 8, Stockholm SE-10044, Sweden

ARTICLE INFO

Keywords:
Multi-stage
Kirigami structure
Drop-weight impact tests
Numerical simulation
Energy absorption

ABSTRACT

As a typical energy-absorbing structure, the thin-walled structure dissipates impact energy through the formation of plastic hinges and material failure. The geometric configuration of the energy-absorbing structure deeply influences its response to impact loads. For a certain load curve required by collision scenarios, this study proposes a novel design method for approximating a continuous impact load curve with discretized ones. Based on kirigami structures, the conceptual framework integrates multi-module and multi-stage designs to regulate segmental stiffness through theoretical analysis, thereby achieving the desired curve approximation. The effectiveness of the proposed kirigami-based multi-stage energy absorption structure (KMS) is validated by drop-weight impact tests and numerical simulations. Findings demonstrate that the KMS effectively dissipates impact energy in a progressive manner, aligning with the desired load curve and inducing stable and orderly structural deformation under axial impact. Through appropriate parameter design, the deformation mode and the inducing effect of the kirigami structure can be managed, enabling the structure's adaptability to diverse collision scenarios.

1. Introduction

Energy-absorbing (EA) structure is widely implemented in aerospace, automobile, rail vehicle and so on [1–3]. Under impact load conditions, EA structures can dissipate impact energy through the plastic deformation, and provide passive safety protection for the vehicle. The thin-walled tubular structure benefits from its lightweight and great designability and has been widely studied [4–6]. The initial peak force (IPF) and the specific energy absorption (SEA) are the main energy absorption characteristics of thin-walled tubular structures, and are also crucial indicators for the crashworthiness evaluation. In general, as the stiffness of a structure increases (usually accompanied by a larger mass), the energy absorption capability also increases, along with an increase in the IPF. A large IPF is disadvantageous to the structural crashworthiness, and an ideal crashworthiness structure should exhibit a low IPF and a large SEA. Therefore, in the design process of EA structures, the IPF and the SEA are a pair of design contradiction, which are more prominent for lightweight EA structures.

In response to the aforementioned design contradiction, researchers have conducted extensive studies on EA structures, as illustrated in Fig. 1. Early researchers primarily concentrated on the investigation of energy absorption characteristics of tubular thin-walled structures, emphasizing geometric configurations (configuration methods), including circular tubes [20,21], rectangular tubes [22–24], triangular tubes [25–27], polygonal tubes [28], and multi-cell tubes [9,29], whose sections are uniform or tapered [8,30]. All of the above configurations exhibit a high IPF, even though the energy absorption efficiency is significant. In comparison to single-cell tubes, the design of multi-cell tubes has been shown to enhance the energy absorption performance of structures [7,27,31]. Bio-inspired design can reduce both the initial peak force and load fluctuations [29,32,33]. Additionally, nesting multiple thin-walled hollow tubes [10,34] can achieve a multi-step energy absorption response. Hybrid methods stand as one of the essential methods to improve the crashworthiness. Lykakos [11] proposed a hybrid geometry, demonstrating superior energy absorption compared to the square tube or the circle tube. Foam-filled structures [12,35,36] are also commonly employed as a hybrid method to enhance structural energy absorption performance. For instance, Xiang [12] found that multi-layer gradient foam-filled structures exhibit higher energy absorption efficiency compared to uniform foam-filled structures or hollow tubes. In addition, wall thickness [37,38] is also an important factor affecting the

* Corresponding author.
E-mail address: weiyuandou@hotmail.com (W. Dou).

https://doi.org/10.1016/j.tws.2024.111920
Received 21 February 2024; Received in revised form 1 April 2024; Accepted 16 April 2024
Available online 17 April 2024
0263-8231/© 2024 Elsevier Ltd. All rights reserved.

Nomenclature

n_{sec}	the number of sides of the cross-sectional geometric shape
N	the number of modules
a_1, a_2, a_3	side lengths of cross-section (mm)
d_1, d_2, d_3	diameters of circular cross-section (mm)
θ_1, θ_2	angles between inclined plates (°)
l_1, l_2	widths of the inclined plates (mm)
D	diameter of the circular tube (mm)
t	wall thickness (mm)
l_t	length of the transition segment (mm)
l_{CT}	length of the circular tube (mm)
$E_{k\_polygon}$, E_{k_circle}	energy dissipation of the kirigami structure (J)
$E_{t\_polygon}$, E_{t_circle}	energy dissipation of the transition segment (J)
E_{CT}	energy dissipation of the circular tube (J)
d_k, $d_{t\_polygon}$, d_{t_circle}, d_{CT}	effective crushing stroke of each segment (mm)
$MCF_{k\_polygon}$, MCF_{k_circle}	mean crushing force of the kirigami structure (kN)
$MCF_{t\_polygon}$, MCF_{t_circle}	mean crushing force of the transition segment (kN)
MCF_{CT}	mean crushing force of the circular tube (kN)
IPF	initial peak force (kN)
SEA	specific energy absorption (kJ/kg)
MCF	mean crushing force (kN)
PCF	peak crushing force (kN)
CFE	crushing force efficiency (/)
ECS	effective crushing stroke (mm)

mechanical properties of energy absorption structures. For example, Liang [13] found that the hybrid design strategy of CFRP-Al multi-cell tubes with variable thickness can effectively increase the specific energy absorption of structures and improve the bending instability. Therefore, configuration methods, involving the change of the geometry or combining multiple structures, can improve the energy absorption characteristics of structures. However, the control over the structural crashworthiness remains limited with changes in geometric shapes, and the issue of excessive IPF persists.

Imperfection methods aim to reduce the IPF by introducing the localized structure that induces deformation. One form of this method involves induced imperfections, such as introducing slits [19,39], holes [40,41], grooves [18,42], or windows [17,43] in thin-walled tubes. This approach not only lightens the weight of the structure but also effectively lowers its initial stiffness, consequently reducing the IPF. Additionally, the inherent imperfections in the structure may lead to uncontrollable deformation modes. Another form includes corrugated metal tubes [14,44,45] and kirigami structures [15,46–48], which exhibit excellent characteristics in terms of smooth loads and reducing the IPF. The introduction of folds decreases the initial stiffness while preserving the structural integrity, allowing better control over subsequent deformation modes.

In summary, traditional thin-walled tubular structures exhibit a typical response with a noticeable IPF (illustrated by the red line in Fig. 2). EA structures with an ideal distribution of structural stiffness can achieve a smooth and gradual rise followed by a stable plateau in the force–displacement response (depicted by the blue line in Fig. 2). Taking into account various constraints such as design and manufacturing, a discrete approach can be used to approximate the continuous target curve, essentially designing the structure in the form of a segmented variable stiffness to obtain a discrete multi-stage force–displacement curve (depicted by the green line in Fig. 2). Additionally, the advances in additive manufacturing technology [49] provide feasibility for designing structures with complex features, particularly complex surfaces [50] and non-uniform wall thicknesses [51].

This study proposes a design method for approximating a continuous impact load curve with discretized ones based on the kirigami structure, which can achieve crashworthiness design of energy absorption structure under specific collision scenario. The conceptual framework integrates multi-module and multi-stage designs to regulate segmental stiffness, thereby achieving the desired curve approximation. The mean crushing force formula of kirigami structures is derived to guide the design. In addition, the proposed energy absorption structure based on the design method in this work provides a hybrid design strategy for kirigami structures and pure circular tubes. By ensuring the integrity of the structure, the sequential and stable deformation of the structure can be managed, which can effectively reduce the initial peak force and improve the energy absorption efficiency. The rest of this study is organized as follows: Section 2 describes the design method and provides the theoretical analysis of the mean crushing force of kirigami structures; In Section 3, a kirigami-based multi-stage energy absorption structure (KMS) is designed based on the design method, and drop-weight impact tests and numerical simulations are conducted to investigate the structure; Section 4 discusses the influence of design parameters on the proposed structure. Section 5 summarizes this study.

2. Structural design

For an ideal EA structure, aiming to reduce the IPF, enhance SEA, and minimize impact acceleration, it is typically desirable for its force–displacement response to express as an ideal curve characterized by a smooth and gradual rise followed by a stable plateau (illustrated by the blue curve in Fig. 2). However, achieving the curve is often challenging. To facilitate design and manufacturing, the ideal curve can be approximated using a multi-stage force–displacement curve. The multi-stage force–displacement response is composed of multiple discrete plateau forces. In terms of structural design, it is possible to control the structural stiffness distribution to obtain various plateau force responses. The introduction of folds in kirigami structures allows for a smoother plateau and excellent peak clipping. The stiffness of kirigami structure can be effectively controlled by adjusting geometric parameters of the kirigami structure. Essential geometric parameters affecting the stiffness of kirigami structures include the number of sides n_{sec} of the cross-sectional geometric shape, side lengths (a_1, a_2, a_3), angles between inclined plates (θ_1, θ_2), and widths of the inclined plates (l_1, l_2).

In terms of the evolution of geometric configurations, kirigami structures are obtained by introducing folds into thin-walled structures with uniform cross-sections, as depicted in the Fig. 3. As n_{sec} approaches infinity, the cross-sectional shape transitions from a polygon to a circle. When θ approaches 180°, the kirigami structure can transform into a thin-walled structure with a uniform cross-section. Simultaneously occurring in both above cases, the kirigami structure can transition into a circular tube.

Considering the relatively stable load of kirigami structure during collapse [15,52], the mean crushing force (MCF) and the effective crushing stroke (ECS) are employed to describe its force–displacement response. To investigate the effect of geometric parameters on the MCF, this study derives a theoretical analytical formula for the MCF. The geometric parameters satisfy certain conditions: $a_2 > a_1$, $a_2 > a_3$, $0 < \theta < 180°$, $d_2 > d_1$, $d_2 > d_3$, $n_{sec} \geq 3$. For a kirigami structure with a regular polygonal cross-section, the geometric parameters satisfy a certain condition, as shown in Eqs. (1) and (2):

$$\theta = \theta_1 + \theta_2 = \arccos\left(\frac{a_2 - a_1}{2l_1}\tan\frac{(n_{sec}-2)\pi}{2n_{sec}}\right) + \arccos\left(\frac{a_2 - a_3}{2l_2}\tan\frac{(n_{sec}-2)\pi}{2n_{sec}}\right) \quad (1)$$

$$a_2 = \frac{2l_1\cos\theta_1}{\tan(n_{sec}-2)\pi/2n_{sec}} + a_1 = \frac{2l_2\cos\theta_2}{\tan(n_{sec}-2)\pi/2n_{sec}} + a_3 \tag{2}$$

For a kirigami structure with a circular cross-section, considered as an extreme type, the geometric parameters satisfy the condition specified in Eqs. (3) and (4):

$$\theta = \theta_1 + \theta_2 = \arccos\left(\frac{d_2 - d_1}{2l_1}\right) + \arccos\left(\frac{d_2 - d_3}{2l_2}\right) \tag{3}$$

$$d_2 = 2l_1\cos\theta_1 + d_1 = 2l_2\cos\theta_2 + d_3 \tag{4}$$

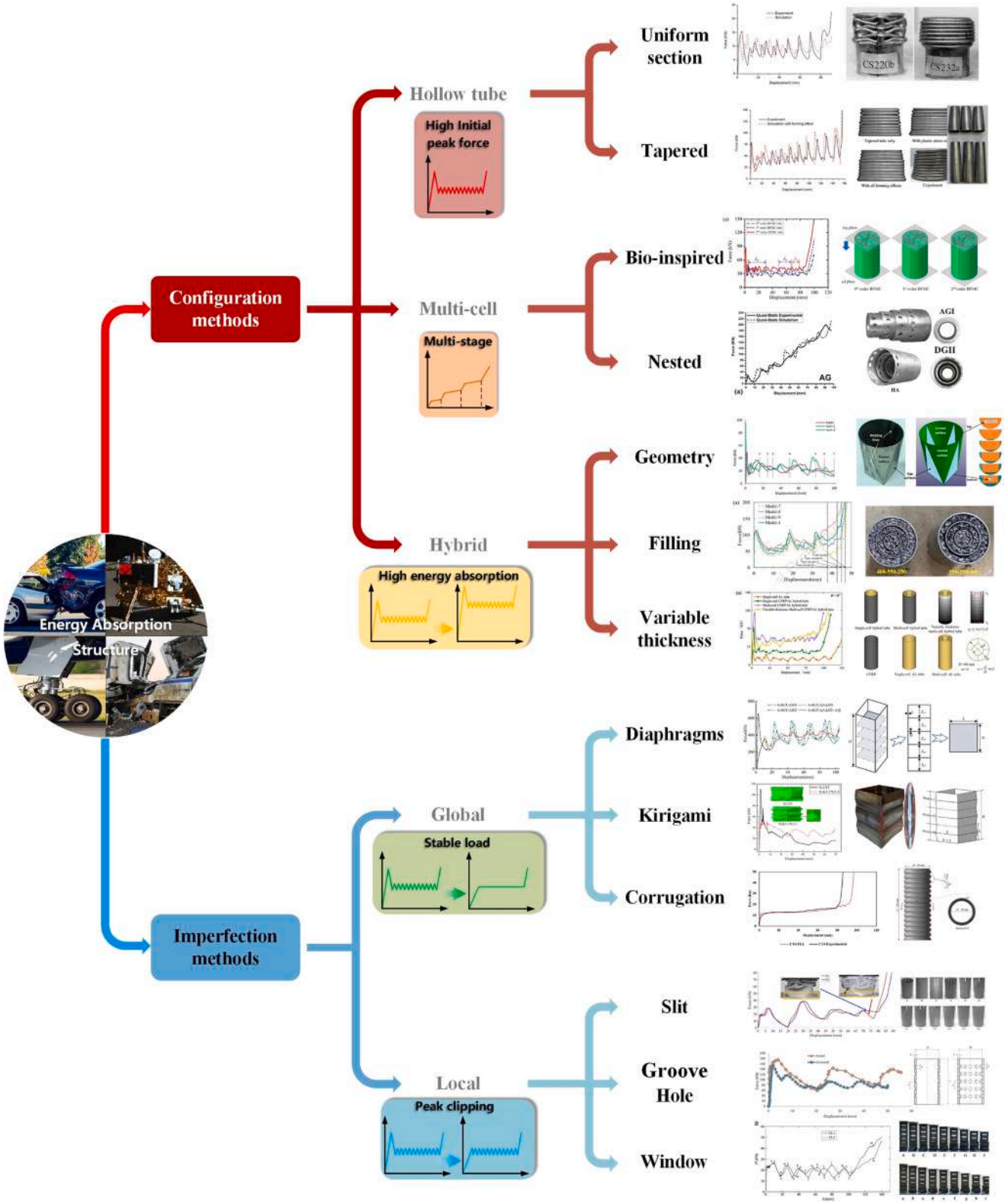

Fig. 1. The design of energy absorption structures: Uniform section [7]; Tapered [8]; Bio-inspired [9]; Nested [10]; Geometry [11]; Filling [12]; Variable thickness [13]; Corrugation [14]; Kirigami [15]; Diaphragms [16]; Windows [17]; Grooves [18]; Slits [19].

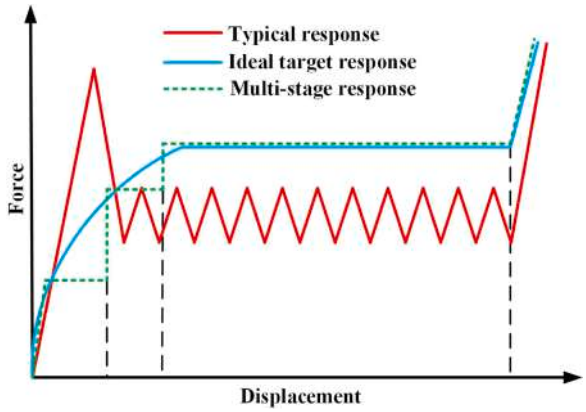

Fig. 2. Different force–displacement responses.

The kirigami structure exhibits an extensional deformation mode (EM) [17,53] during collapse, the plastic energy dissipation mainly involves the bending of stationary plastic hinges and the shape distortion of the panel, as illustrated in Fig. 4. For a kirigami structure with a regular polygonal cross-section, the energy dissipation of N basic modules is given by Eq. (5), with the MCF expressed in Eq. (7). Additionally, d_k represents the ECS.

$$E_{k\_polygon} = n_{sec} N M_p \left(a_1\theta_1 + a_2(\theta_1+\theta_2) + a_3\theta_2 + c_1(\pi - 2\eta_1) + c_2(\pi - 2\eta_2) + 4\frac{c_1^2}{t}\psi(1-\sin\alpha_1) + 4\frac{c_2^2}{t}\psi(1-\sin\alpha_2) \right) \tag{5}$$

$$d_k = (l_1\sin\theta_1 + l_2\sin\theta_2 - 2t)N \tag{6}$$

$$\mathrm{MCF}_{k\_polygon} = E_{k\_polygon} \,/\, d_k \tag{7}$$

For a kirigami structure with a circular cross-section, the energy dissipation of N basic modules is given by Eq. (8), with the MCF expressed in Eq. (9).

$$E_{k\_circle} = n_{sec} N M_p \pi \left(d_1\theta_1 + d_2(\theta_1+\theta_2) + d_3\theta_2 + \frac{4l_1^2}{t}(1-\sin\alpha_1) + \frac{4l_1^3}{3d_1 t}(1+\cos 2\alpha_1) + \frac{4l_2^2}{t}(1-\sin\alpha_2) + \frac{4l_2^3}{3d_2 t}(1+\cos 2\alpha_2) \right) \tag{8}$$

$$\mathrm{MCF}_{k\_circle} = E_{k\_circle} \,/\, d_k \tag{9}$$

The derivation process for Eqs. (5) and (8) is provided in Appendix.

The above-mentioned analytical formulas reveal that, as n_{sec} decreases, θ increases, l_1 and l_2 decrease, and a_1 and a_3 increase, the MCF gradually increases. By combining different geometric parameters, various kirigami structures with different stiffness can be constructed, exhibiting different MCF. In response to design requirements in a certain collision scenario, the theoretical analytical formulation is utilized to guide the design of the kirigami structure by controlling the geometrical parameters according to the previously described laws in order to obtain a multi-stage response that approximates the target curve.

The thin-walled circular tube represents an extreme type of the kirigami structure, it is widely employed in the design of EA structures due to its simple structure, easy manufacturing, and significant EA efficiency. Axial symmetric deformation (the accordion mode), non-symmetric one (the diamond mode), and hybrid one [54] are the primary deformation modes of the thin-walled circular tube under the impact load. Abramowicz and Jones established corresponding theoretical analytical formulas for the collapse deformation of circular tubes [55]. The energy dissipation of the thin-walled circular tube is given by Eq. (10), with the MCF expressed in Eq. (12). The ECS is denoted as d_{CT}.

$$E_{CT} = 62.88 M_p (D/t)^{0.33} l_{CT} \tag{10}$$

$$d_{CT} = \left(0.86 - 0.568(t/D)^{0.5}\right) l_{CT} \tag{11}$$

$$\mathrm{MCF}_{CT} = E_{CT} \,/\, d_{CT} \tag{12}$$

Additionally, the connection of general kirigami structures to circular tubes requires the hybrid geometry (the transition segment). The theoretical analytical formula for the MCF of the transition segment is supplemented by simplifying the transition segment to the conical tube, and the specific derivation is referred to literatures [8,56]. For the transition segment connecting the polygon and the circle, the energy dissipation is given by Eq. (13), with the MCF expressed in Eq. (15). Where $d_{t\_polygon}$ and l_t. are the ECS and the length of the transition segment.

$$E_{t\_polygon} = 62.88 M_p ((n_{sec} a_3/\pi + D)/2t)^{0.33} l_t \tag{13}$$

$$d_{t\_polygon} = \left(0.86 - 0.568(2t/(n_{sec} a_3/\pi + D))^{0.5}\right) l_t \tag{14}$$

$$\mathrm{MCF}_{t\_polygon} = E_{t\_polygon} \,/\, d_{t\_polygon} \tag{15}$$

For the transition segment connecting two circles, the energy dissipation is given by Eq. (16), with the MCF expressed in Eq. (18). Where d_{t_circle} is the ECS,

$$E_{t\_circle} = 62.88 M_p ((d_3 + D)/2t)^{0.33} l_t \tag{16}$$

$$d_{t\_circle} = \left(0.86 - 0.568(2t/(d_3 + D))^{0.5}\right) l_t \tag{17}$$

$$\mathrm{MCF}_{t\_circle} = E_{t\_circle} \,/\, d_{t\_circle} \tag{18}$$

The design flow chart is illustrated in Fig. 5. The structural design is carried out based on given target force–displacement curve in a certain scenario. The target curve is discretized into n segments and the number of structural segments. Two design cases are considered, including the conventional design case and the hybrid design one. For the former case, the structure is divided into n segments. The initial geometric parameters of each kirigami structure are inputted. The MCF and ECS for each segment are calculated by using the derived theoretical analysis formula. It is worth noting that the corresponding calculation formula

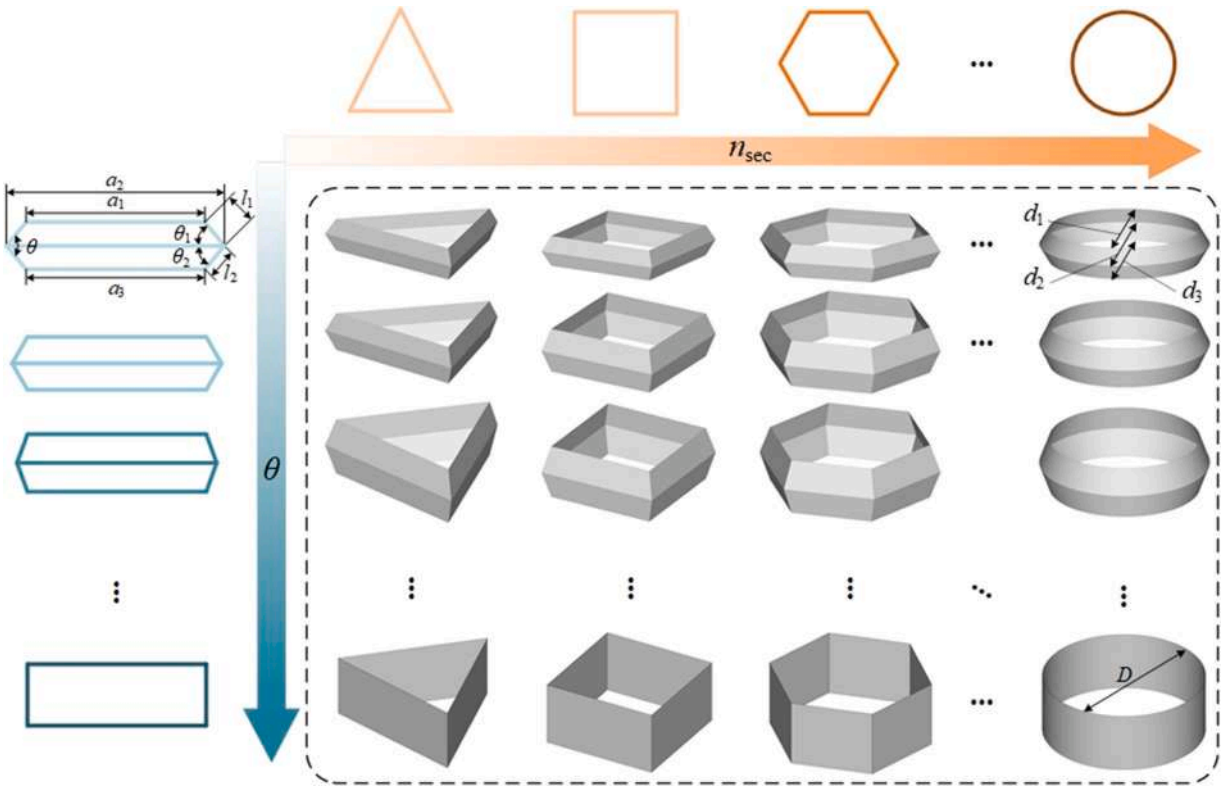

Fig. 3. Variation of geometric parameters of krigami structure.

needs to be selected according to the cross-sectional shape of the kirigami structure. The calculated force–displacement curve is evaluated against the discrete multi-stage one. If it does not meet the requirements, it is necessary to readjust the geometric parameters. Kirigami structures for the design case can be combined in order of magnitude of the MCF, see Fig. 4. For the latter case, when constrained by requirements such as mass or SEA, an extreme type of the kirigami structure, namely the circular tube, is selected to meet the design requirements. Compared to general kirigami structures, circular tubes typically exhibit higher MCF and SEA. In the hybrid design case, there may be connections between different cross-sectional shapes, necessitating the introduction of hybrid geometry (Transition segment II). The transition segment connects the kirigami structure I and the circular tube III by transitioning between two geometric cross-sectional shapes. The transition segment achieves the connection between two geometric cross-section through lofting [57], and the two geometric cross-sectional shapes can be either identical or different. Furthermore, the hybrid design case can be divided into two types. In the first one, the structure is divided into n segments,

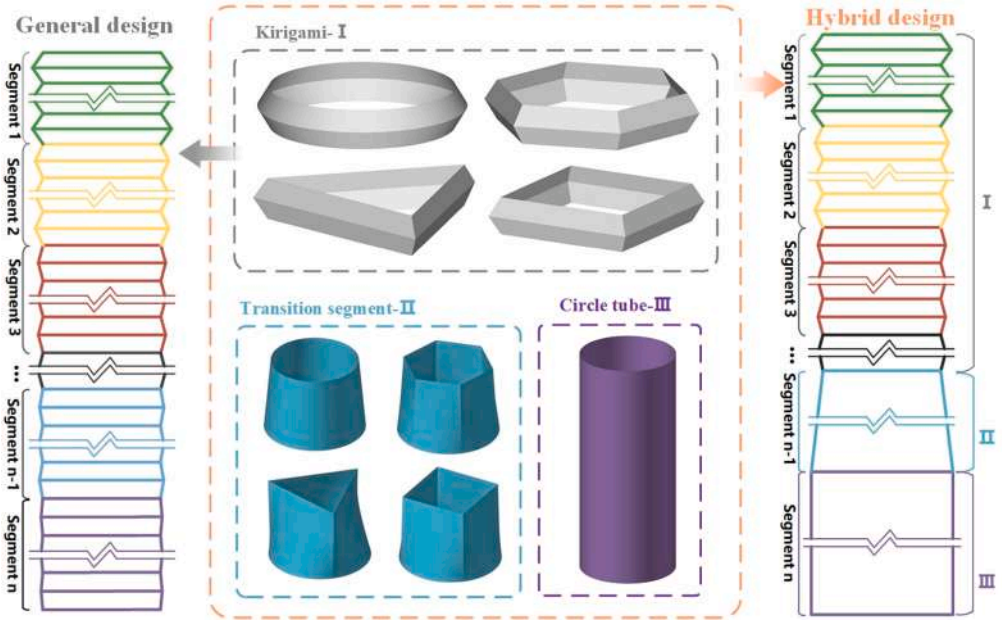

Fig. 4. General design and hybrid design.

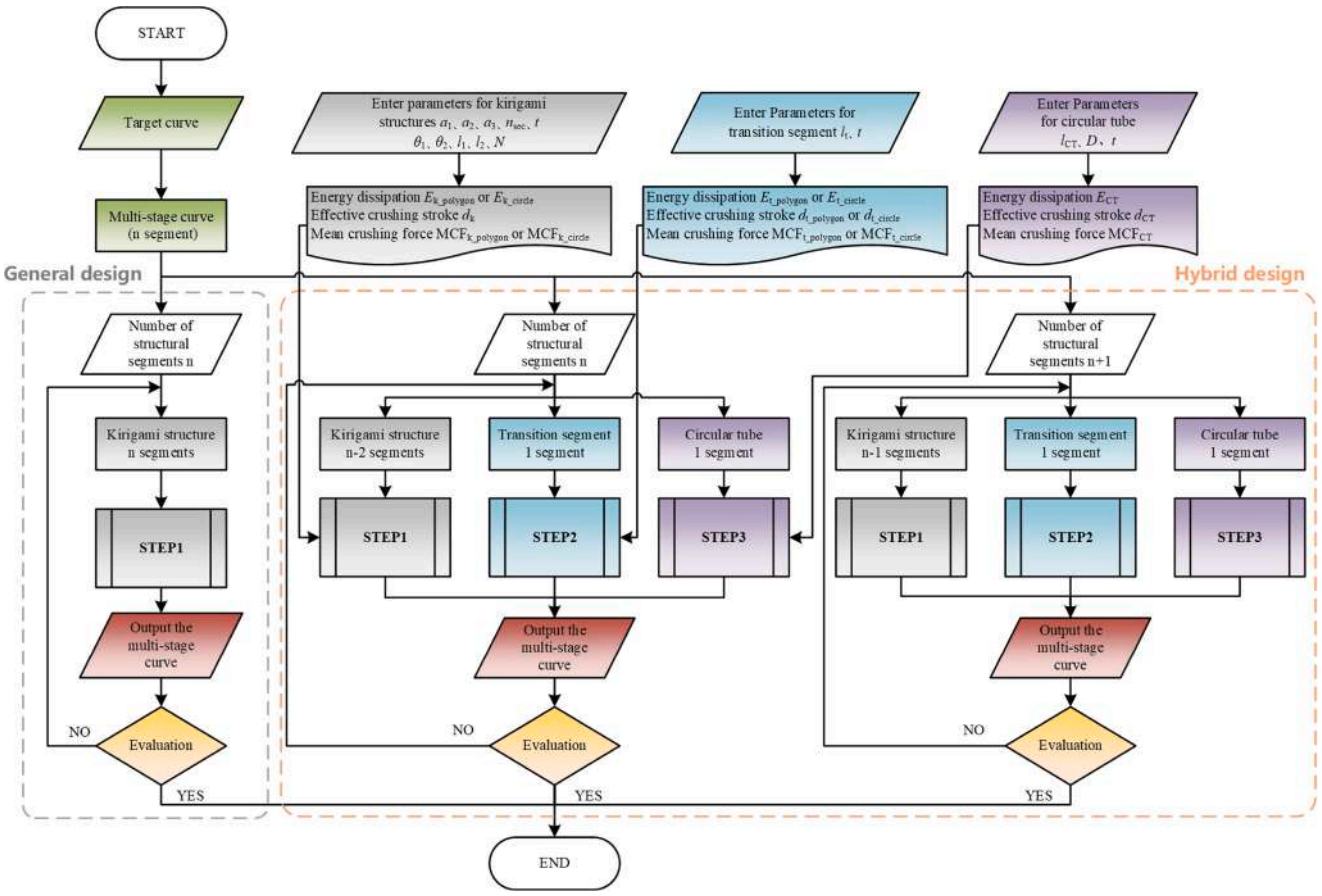

Fig. 5. Design flow chart.

with n-2 segments for I, 1 segment for II, and 1 segment for III. In the second one, the structure is divided into $n + 1$ segments, with n-1 segments for I, 1 segment for II, and 1 segment for III. In this case, II and III are combined into one segment, taking into account the fact that there is no significant difference in the MCF between II and III for the same wall thickness.

3. Test and finite element modeling

3.1. Description of a two-stage KMS

In this study, the above design method is used to design the structure in response to the given collision scenario. Different collision scenarios correspond to different target energy absorption curves, and the plateau force $F_{plateau}$, the effective crushing stroke (ECS), and the absorbed energy E are the key information of the target curve. Assuming that there exists a target curve (the red line in Fig. 6), the crushing force increases from 0 to 18 kN in the range of ECS from 0 to 45 mm, and the plateau force is 18 kN in the crush stroke from 45 to 135 mm, while the absorbed energy E is not less than 2200 J. The specific design requirement is illustrated in Eq. (19). The target curve exhibits a slow growth of the crush force from 0 to the plateau force for the initial 1/3 of the ECS, which reduces the impact acceleration and the initial peak force, while maintains a stable plateau force in the remaining ECS.

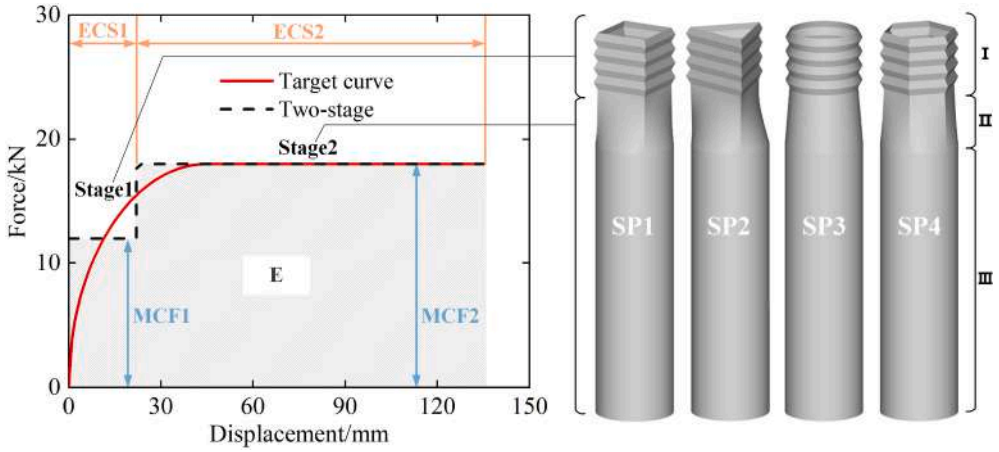

Fig. 6. The target curve and two-stage curve.

Table 1
The parameter of specimens.

NO.	Section shape	a_1/mm	a_2/mm	t/mm	l/mm	θ/°	N	l_t/mm	l_{CCT}/mm	D/mm
SP1	square	27.5	31.0	1	4.138	130	4	30	140	40.5
SP2	triangle	36.7	41.3	1	3.978	141	4	30	140	40.5
SP3	circle	35.0(d_1)	39.5(d_2)	1	4.373	118	4	30	140	40.5
SP4	hexagon	18.3	20.7	1	4.287	122	4	30	140	40.5

$$Designrequirementsto\begin{cases} F_{plateau} = 18\text{kN} \\ \text{ECS} = 135\text{mm} \\ \text{E} \geq 2200\text{J} \end{cases} \tag{19}$$

According to the design method of Section 2, the study takes the two-stage energy absorption as an example, and the continuous curve is discretized into a two-stage curve, with the first stage exhibiting the mean crushing force MCF1 of 12 kN and the effective crushing stroke ECS1 of 22 mm, while the other stage exhibits the mean crushing force MCF2 of 18 kN and the effective crushing stroke ECS2 of 123 mm. Additionally, the expected absorbed energy E is 2478 J (the shaded area in Fig. 6). The energy-absorbing structure is divided into three segments by the hybrid design, including a kirigami structure I, a transition segment II and a circular tube III, in which I dominates the energy absorption of stage1, II and III dominate the energy absorption of stage2. Different kirigami structures with various cross-section are connected with circular tubes to design the kirigami-based multi-stage energy absorption structure (KMS). Considering the complexity of geometric parameters for kirigami structures, we set $l = l_1 = l_2$, $a_1 = a_3$, $\theta_1 = \theta_2 = 1/2\theta$ to simplify the issue. The parameters are shown in Table 1. Subsequently, drop-weight impact tests and numerical simulations will be conducted to analyze the KMS.

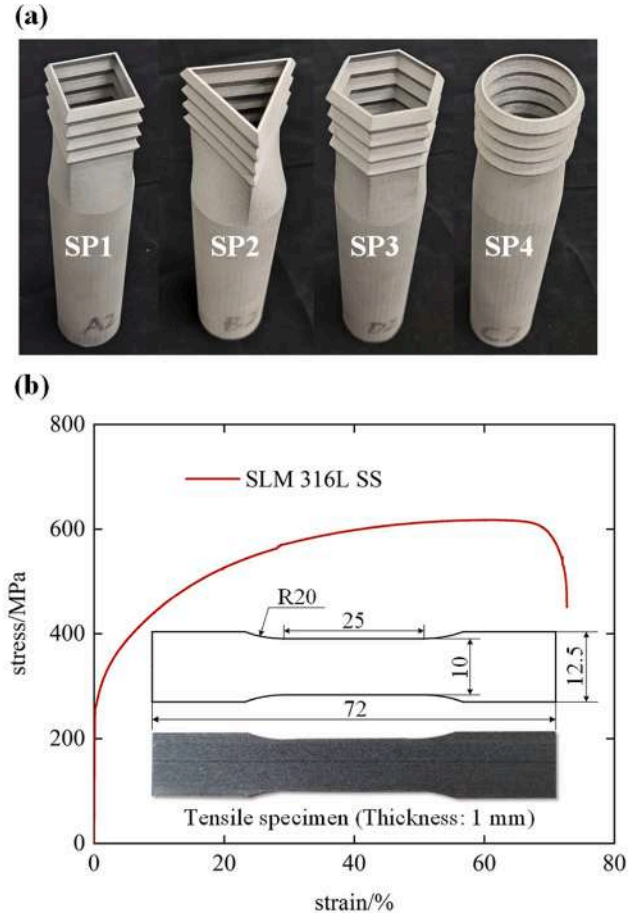

Fig. 7. Material and specimen: (a)Specimens; (b) Engineering stress-strain curve of SLM 316L SS and size of the tensile specimen.

Table 2
Material parameters of SLM 316L SS.

Material	Density ρ /(kg/m^3)	Young modulus E /GPa	Poisson's ratio ν	Yield strength σ_y /MPa
SLM 316L SS	7850	207.9	0.33	253.75

3.2. Material and specimens

The specimens were manufactured by SLM machine, and the manufacturing process parameters were set according to supplier's suggestions. The laser power is 215 W, the scanning speed is 900 mm/s, the hatch spacing is 150 μm, and the layer thickness is 30 μm. In addition, incomplete melting may be formed during the manufacturing process, resulting in the formation of irregular, large-size voids between the layers of the material [58], which will affect the mechanical properties of 316L stainless steel. Therefore, specimens are subjected to vacuum heat treatment to enhance the fracture elongation. Four structures with different cross-section are fabricated, as illustrated in Fig. 7a. Subsequently, standard tensile tests are conducted on specimens according to GB/T228.1-2010 to obtain material properties. The specific parameters of the material are detailed in the Table 2, and the engineering stress-strain curve for the material is depicted in Fig. 7b.

3.3. Drop-weight impact test

Fig. 8 illustrates the setup for the drop-weight impact test. The drop-weight impact test is conducted using an impact testing machine, equipped with a computer control and data acquisition system. The impact energy and velocity range of the machine are 1260 J~30,000 J, 2 m/s~7.67 m/s, respectively. The sampling frequency is 500 kHz. Additionally, a high-speed camera is employed to make it easier to gain a clear observation of the specimen's deformation process upon impact. A die with a boss is employed and securely bolted to the impact test bench. The impactor has a weight of 730 kg, and the initial impact speed is set at 2.84 m/s. Throughout the test, the force–displacement sensor provided measurements of the crushing force and displacement experienced by specimens.

3.4. Finite element modeling

To evaluate the mechanical behavior of the proposed KMS under axial impact load, the numerical simulation using the finite element modelling (FEM) is implemented. As seen in Fig. 9(a), the FE model is discretized using the four-node Belytschko–Tsay shell element and the simulation is performed using the single-point integration algorithm. In such large deformation processes [59], five integration points are often defined along the thickness direction of shell elements to minimize hourglass energy and also to enhance computation accuracy. In order to select the appropriate mesh size, the mesh sensitivity analysis is carried out. Fig. 9(b) shows that when the mesh size is less than 1 mm, MCF of the proposed KMS remains relatively stable. To balance the efficiency and accuracy of the computation, a mesh size of 0.75 mm was selected

Fig. 8. Drop-weight impact test setup.

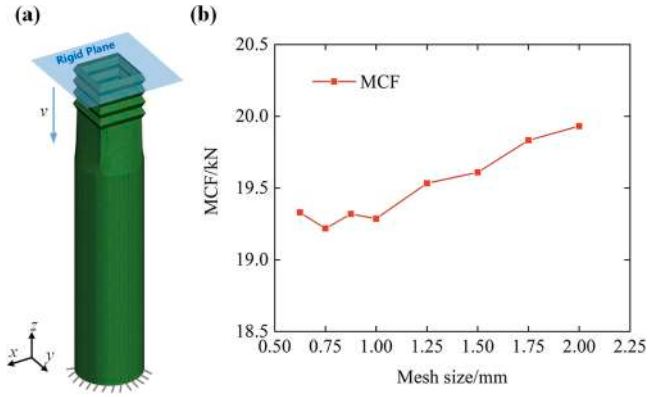

Fig. 9. Finite element modeling: (a)Meshing;(b) The mesh sensitivity analysis.

Table 3
Crashworthiness indicators [5].

Indicator	Expression	Characteristics
Initial peak force, IPF	/	IPF is employed to monitor the initial impact acceleration; For instance, in the scenario of a vehicle collision, the initial peak should be minimized or eliminated in order to limit the impact acceleration [60] that will probably result in passenger injuries or even casualties.
Energy absorption, EA	$EA(d) = \int_0^d F(s)ds$	EA is used to determine the energy absorption capability of a structure with the identical mass. It can only depict the change of energy, but not the load condition;
Specific energy absorption, SEA	$SEA(d) = \frac{EA(d)}{m}$	SEA is used to determine a structure's energy absorption capability and is also employed for structures with different mass. The higher the SEA value, the better.
Mean crushing force, MCF	$MCF(d) = \frac{EA(d)}{d}$	It indicates the average load within the effective crushing stroke d;
Peak crushing force, PCF	/	The maximum crushing force within the effective crushing stroke;
Crushing force efficiency, CFE	$CEF(d) = \frac{MCF(d)}{PCF(d)}$	It can be used to determine the relationship between the average load and the maximum force within the effective crushing stroke, as well as load fluctuation. A higher CFE is advantageous for increasing the structure's energy absorption capability

Note: d is the effective crushing stroke (ECS) [19].

for finite element analysis. The nonlinear explicit dynamics computations in this section are performed using the LS-DYNA solver. The upper pressing plate is configured to have a rigid property, with an initial velocity of 2.84 m/s and a constant mass of 730 kg. The HMT 's bottom end uses full constraint. LS-DYNA's keyword, *CONTACT_AUTOMATICT_SURFACE_TO_SURFACE, is employed to simulate the contact between the rigid plate and the HMT. Additionally, *CONTACT_AUTOMATICT_SINGLE_SURFACE, is used to simulate the contact formed by the thin-walled structure's inherent plastic deformation. The friction coefficient is 0.1. The constitutive model, *MAT_PIECWISE_LINEAR_PLASTICITY in LS-DYNA, is utilized.

3.5. Results analysis and validation

In this study, crashworthiness indicators [61] are used to evaluate the energy absorption capacity of KMS with different parameters, as shown in Table 3. Comparing the test with finite element simulations reveals a good agreement in both the impact deformation process and the force–displacement curve, as shown in Figs. 10 and 11. The relevant crashworthiness indicators are presented in Table 4. The error of experiment and simulation is about 5–10 %. Therefore, the accuracy of the finite element model established in this study has been validated, and it can be utilized to simulate other structures and assisting in the analysis of experimental results. Moreover, under axial impact loads and the current geometric dimensions, the specimens exhibit a two-stage force–displacement response, mainly due to the fact there is no significant difference in the MCF between the transition segment and the circular tube. As shown in Fig. 12, the force–displacement curve from the experiment closely aligns with the two-stage curve in terms of trend. The fluctuation in load during the second plateau is considered a normal occurrence, attributed to the progressive deformation of the circular tube and the gradual formation of plastic hinges layer by layer.

3.5.1. Deformation mode

The mechanical response and deformation mode of KMS were analyzed through a combination of drop-weight impact tests and numerical simulations. As illustrated in Fig. 10, it is evident that specimens exhibit the ordered deformation mode in the kirigami structure. This process induced the sequential development of plastic hinges in the transition segment and the circular tube. For SP1, the folding of the kirigami structure initiated in the first module and the fourth module, followed by the subsequent folding of the two modules situated in the middle. The kirigami structure induced a diamond mode deformation characterized by four-fold in the transition segment. Subsequently, when the second plastic hinge formed, the diamond mode transformed into a three-fold configuration. It is obviously observed that the circular

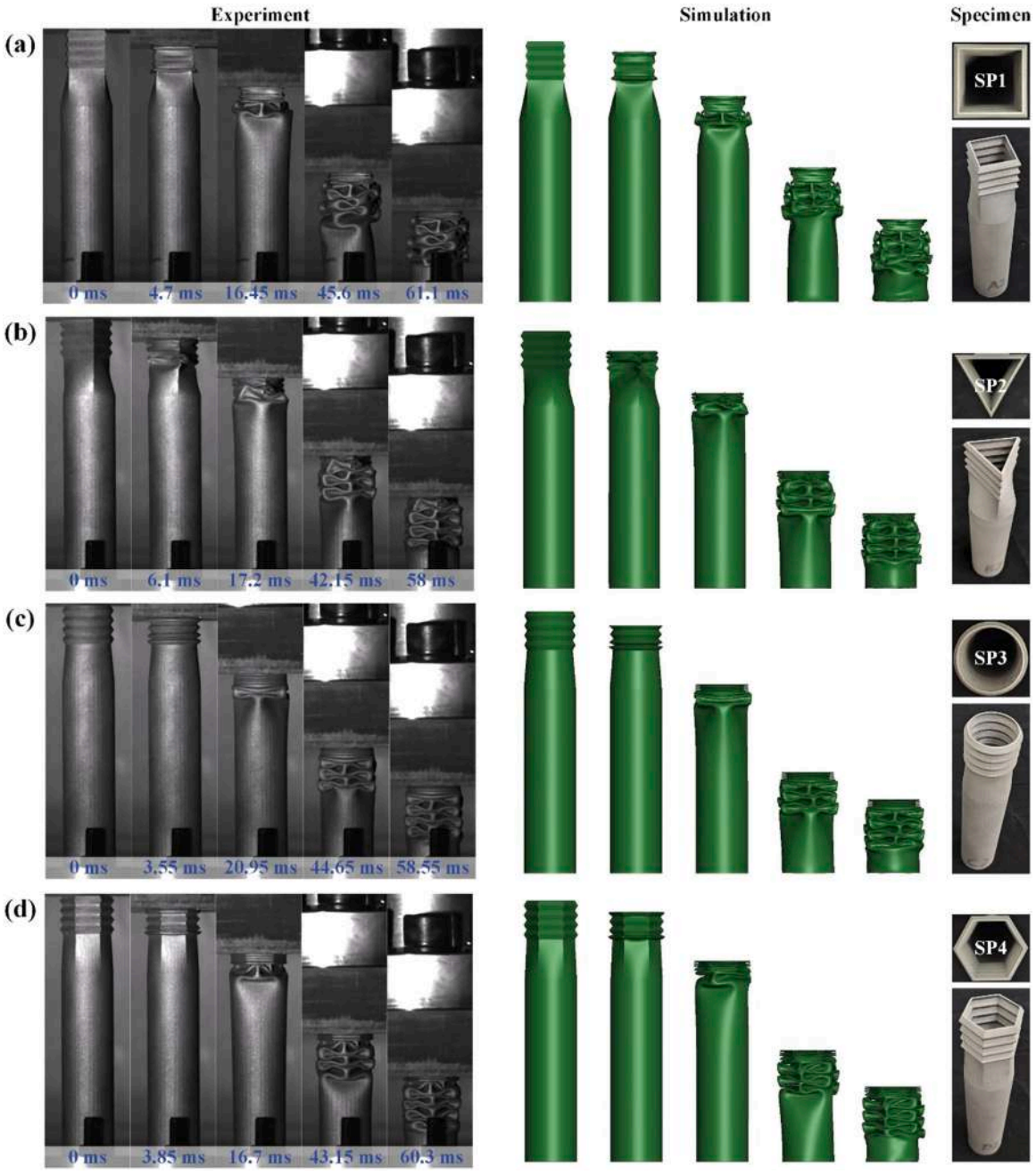

Fig. 10. Comparison of drop-weight impact tests and finite element simulations.

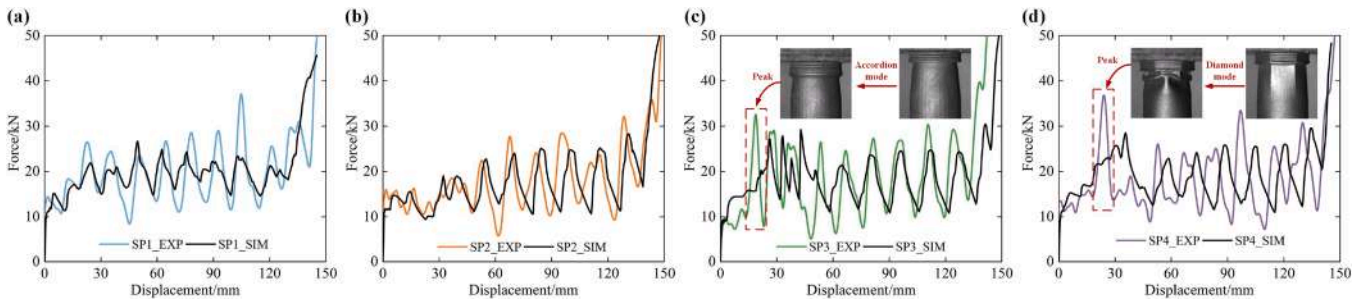

Fig. 11. Force–displacement curves of test and simulation: (a)SP1; (b)SP2; (c)SP3; (d)SP4.

Table 4
Results comparison of experiment and simulation.

NO.	Experiment						Numerical simulation			
	EA/J	*m*/kg	IPF/kN	SEA/(kJ/kg)	CFE/(%)	MCF/kN	IPF/kN	SEA/(kJ/kg)	CFE/(%)	MCF/kN
SP1	2738.576	0.177	14.448	15.516	52.365	19.413	15.196	15.609	48.11 %	18.684
SP2	2560.721	0.175	15.972	14.633	48.976	17.579	14.799	13.807	48.10 %	16.643
SP3	2274.854	0.178	9.909	12.766	52.959	17.238	9.403	13.390	57.55 %	17.504
SP4	2446.480	0.179	13.527	13.673	48.252	17.757	15.174	14.699	63.34 %	18.742

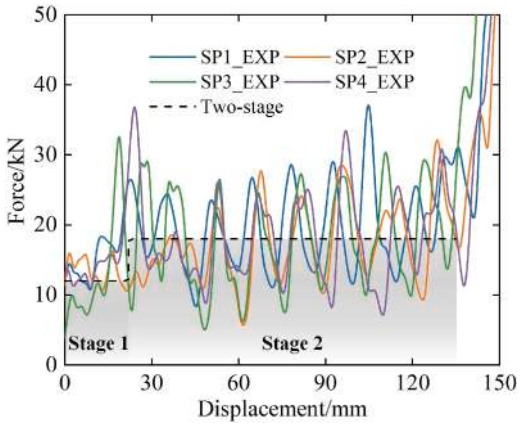

Fig. 12. The two-stage curve and the experimental curve.

tube exhibits a hybrid deformation state, combining four -fold and three-fold modes. Fig. 13a illustrates that the kirigami structure of SP1 primarily exhibits two deformation modes, namely, Inflated Extension Mode (IEM) and Corolla Extension Mode (CEM). However, the CEM results in inadequate folding in the stationary hinge line. Fig. 13b reveals that the kirigami structure of SP2 does not fold according to the stationary hinge line. During the folding process, the top module expands outward, while the bottom module concaves inward. As further folding and deformation occur, the module's corner gradually inclines, inducing a layer of plastic hinge in the transition segment which results in an ordered three-fold diamond mode deformation in the circular tube. As illustrated in Fig. 13c. The kirigami structure of SP3 folds evenly along the stationary hinge line. Subsequently, the transition segment forms a layer of accordion plastic hinge, leading to the transformation of deformation into an ordered 3-fold diamond mode in the circular tube. In the case of SP4, as depicted in Fig. 13d, the kirigami structure also folds evenly, inducing an ordered three-fold diamond mode in the circular tube. Notably, SP4 experiences fracture failure due to the fact that the transition segment is constrained by the kirigami structure with a hexagonal cross-section, which forms inwardly expanding plastic hinge, resulting in structural fracture.

3.5.2. Crashworthiness analysis

Force–displacement curves shown in Fig. 11 demonstrate that KMS with different cross-section shapes exhibit a favorable peak clipping and significant plateaus. As illustrated in Table 4, it can be observed that the SEA of SP1 exhibits the highest SEA among all the specimens, reaching 15.516 kJ/kg. which is 21.5 % larger than the lowest value obtained for SP3. Furthermore, the CFE of SP1, at 52.365 %, is second only to that of SP3. Consequently, SP1, with a square cross-section, exhibits superior performance in terms of the evaluation indicators for energy absorption. Furthermore, it can be observed that as the number of sides n_{sec} increases, the IPF of KMS gradually decreases. Notably, SP3 exhibits the lowest initial peak force, measuring 9.909 kN, which can be attributed that the kirigami structure with circular cross-section are easier to folding deformation due to the absence of inclined stationary hinge lines for bending. Consequently, the circular cross-section demonstrates lower stiffness, resulting in a more remarkable peak clipping.

Additionally, it can be observed that SP3 and SP4 exhibit a remarkable peak after entering the plateau stage. It can be noted that plastic hinges in accordion mode appears in the transition segment during the peak period of SP3, as shown in Fig. 11c. In the case of SP4, the kirigami structure induces the formation of diamond mode plastic hinges in the transition segment, as shown in Fig. 11d. Although the kirigami structure can induce controlled deformation in the transition segment and the circular tube, the kirigami structure with different cross-section yields different force–displacement responses. Notably, the transformation of the deformation mode is disadvantageous to the stability of the load under the current load condition.

4. Discussion

4.1. Study of design parameters

It is observed from Section 3 that the KMS with three-segment structure exhibits a two-stage force–displacement response. However, the fluctuation in the force–displacement curve and the energy absorption performance are influenced by the deformation mode of the KMS. Therefore, an analysis of the effect of design parameters on the KMS with a three-segment configuration is conducted by numerical simulations. Key design parameters for the kirigami structure include the side length of the cross-section (a_1), the width of the inclined plate (l), and the angle between the inclined plates (θ). Numerical simulations are conducted by using a univariate method for the examples. Considering the actual installation dimensions of structures in engineering practice, especially when installed in confined spaces, it is assumed here that the total length of the structure is a constant value of 200 mm. The central diameter of the circular tube is 40.5 mm, with a wall thickness of 0.8 mm, and the number of modules in the kirigami structure is 4. The length of the circular tube is a constant value of 130 mm. The section primarily discusses the parameters a_1, l and θ, with detailed information provided in the Table 5. The analysis from Section 3.5 indicates that the KMS with a square cross-section exhibits relatively superior performance in terms of energy absorption capacity, peak clipping, and load stability. Therefore, kirigami structures with square cross-sections are employed as examples for numerical simulations to explore the effect of design parameters on its performance.

4.1.1. Effect of the side length a_1

Within the range of 22–30 mm for a_1, as the a_1 increases, the plateau force of kirigami structure gradually rises, and the IPF increases gradually. The kirigami structure primarily exhibits the IEM and CEM. For a_1_22, a_1_24 and a_1_26, a "3I + 1C" mode is observed, while a_1_28 and a_1_30 exhibit a "1I + 3C" mode. As shown in Fig. 14, the CEM causes horizontal stationary plastic hinge lines to not fully fold, resulting in a decrease in the plastic deformation energy dissipated. Fig. 15 reveals that with the increase in a_1, the SEA of the structure decreases. Additionally, except for a_1_30, all examples exhibit stable and ordered diamond mode deformation. Fig. 16 shows that a_1_30 exhibits a significant peak at a crushing displacement of approximately 55 mm, where the circular tube of a_1_30 undergoes local buckling during the crushing deformation process, gradually transitioning from a four-fold diamond mode to a three-fold one, and leading to a decrease in plateau force. The

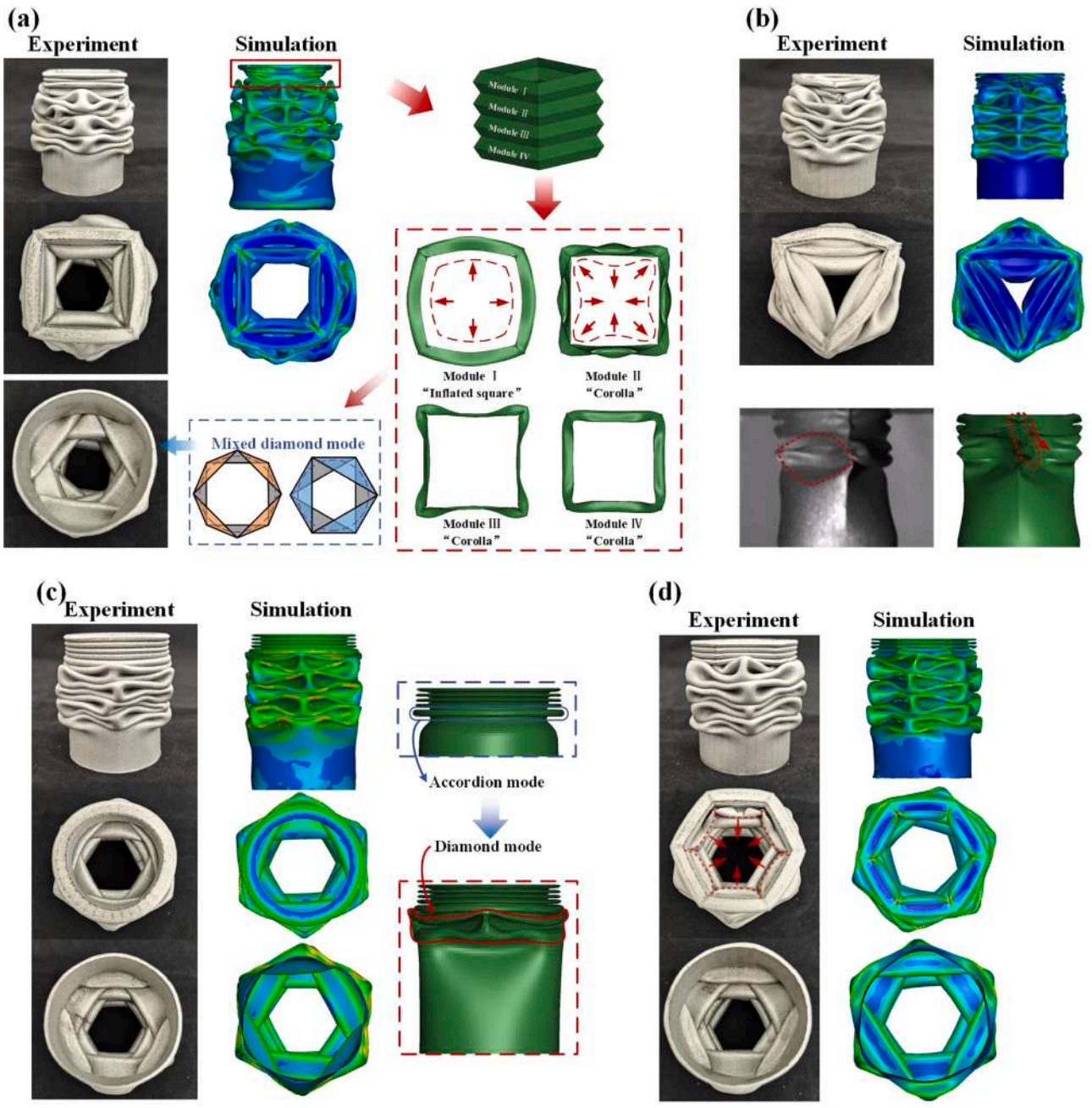

Fig. 13. Deformation mode of specimens: (a)SP1; (b)SP2; (c)SP3; (d)SP4.

larger a_1, the less likely the kirigami structure is to form the IEM and the larger the load fluctuation.

4.1.2. *Effect of the angle between the inclined plates θ*

In the range of 110° to 150° for θ, as θ increases, the plateau force of the folded structure gradually increases, attributed to the increasing stiffness of the kirigami structure. However, with larger θ values, the bending moment of the horizontal stationary plastic hinge line in the kirigami structure increases, leading to insufficient folding deformation and difficulty in forming the IEM. For θ_150, in particular, the folding deformation does not occur as expected along the hinge line, as shown in Fig. 17, and there is a noticeable peak in the initial stage. Additionally, as θ increases, both SEA and IPF exhibit a gradual increasing trend, as illustrated in Fig. 18. Fig. 19 reveals that θ_110 and θ_120 show relatively stable loads in the initial stage, while other examples exhibit significant fluctuations. Within the parameter range, the θ has no significant effect on deformation modes of the transition segment and the circular tube. Excessively large θ make it difficult for the kirigami structure to form the IEM, resulting in a larger initial peak force.

4.1.3. *Effect of the width of the inclined plate l*

In the range of 3.1 mm to 5.1 mm for l, as the l decreases, the plateau force of the kirigami structure gradually increases, and the IPF also increases gradually, attributed to the increasing stiffness of the kirigami structure, as shown in Fig. 20. Smaller values of l result in insufficient folding deformation of the kirigami structure, making it difficult to form the IEM. With the decrease in l, the load fluctuations of the kirigami structure gradually increase. Notably, l_3.1 exhibits a significant initial peak force. As observed in the Fig. 21, there is no clear monotonic relationship for the structural SEA with the variation in l. Among the

Table 5
Parameters of examples.

NO.	a_1 /mm	t/mm	l/mm	θ/°	N	l_{CCT} /mm	D /mm
a_1_22	22	0.8	4.1	130	4	130	40.5
a_1_24	24	0.8	4.1	130	4	130	40.5
a_1_26	26	0.8	4.1	130	4	130	40.5
a_1_28	28	0.8	4.1	130	4	130	40.5
a_1_30	30	0.8	4.1	130	4	130	40.5
θ_110	26	0.8	4.1	110	4	130	40.5
θ_120	26	0.8	4.1	120	4	130	40.5
θ_130	26	0.8	4.1	130	4	130	40.5
θ_140	26	0.8	4.1	140	4	130	40.5
θ_150	26	0.8	4.1	150	4	130	40.5
l_3.1	26	0.8	3.1	130	4	130	40.5
l_3.6	26	0.8	3.6	130	4	130	40.5
l_4.1	26	0.8	4.1	130	4	130	40.5
l_4.6	26	0.8	4.6	130	4	130	40.5
l_5.1	26	0.8	5.1	130	4	130	40.5

examples, l_4.6 has an excellent performance in both SEA and IPF, but during the formation of plastic hinges in the transition segment, l_4.6 forms a plastic hinge at the connection between the transition segment and the circular tube, as indicated by the red line of l_4.6 in the Fig. 20, leading to significant fluctuations in the force–displacement response. The magnitude of l affects the formation of plastic hinges in the transition segment and the fluctuation of the load.

4.2. Thickness gradient

From drop-weight impact tests, it is observed that for KMS with uniform thickness, the peak clipping is evident. However, plateaus of the transition segment and the circular tube are relatively close, resulting in a two-stage force–displacement response for the KMS with three segment structures. Thanks to the additive manufacturing, the proposed KMS can be designed with variable thickness, which will be discussed in this section. Building upon a_1_26, KMS with different thickness gradient distributions is considered. The specific thickness parameters are detailed in Table 6, where t_1 represents the thickness of the kirigami structure, t_2 is the thickness of the transition segment, and t_3 is the thickness of the circular tube.

It is evident that KMS with different thickness gradient distributions exhibits a three-stage force–displacement response, and the simulation results are in good agreement with that of theoretical analysis, as shown in Fig. 22. The kirigami structure achieves stable loading and peak clipping due to introduced imperfections, while the circular tube maintains the stable progressive deformation and the higher SEA. Additionally, the transition segment with a hybrid geometry combines the kirigami structure and the circular tube, achieving both peak clipping and high energy absorption. In terms of crashworthiness indicators, with the increasing thickness gradient, the SEA of the KMS gradually increases, while the IPF and the CFE decrease, as shown in Figs. 23 and 24.

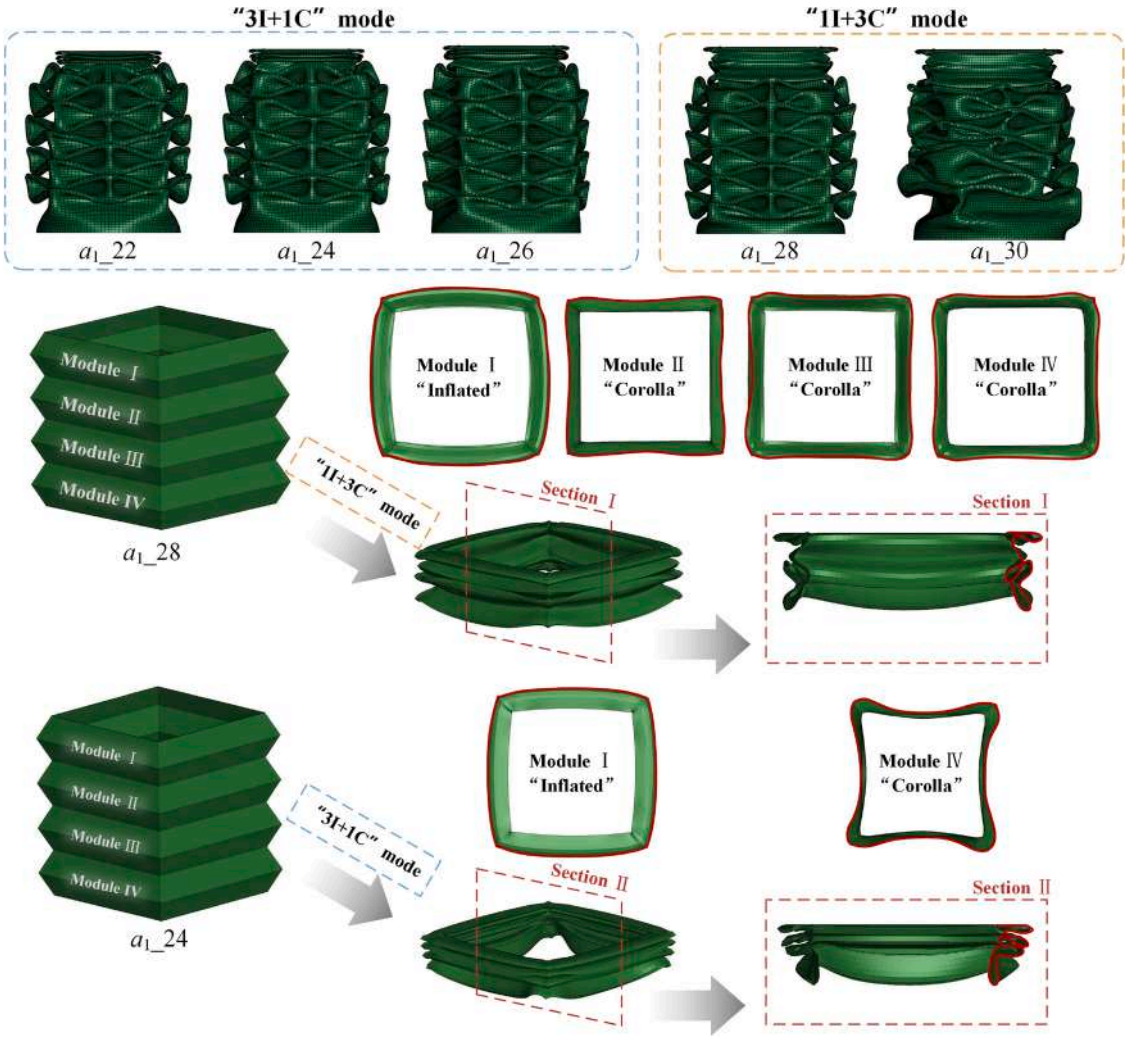

Fig. 14. Deformation mode of the kirigami structure with different a_1.

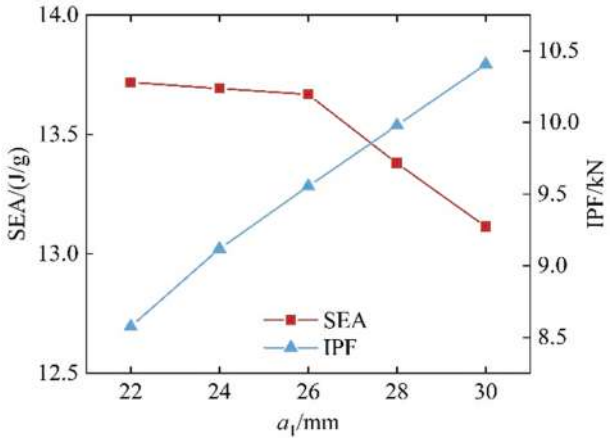

Fig. 15. Crashworthiness indicators with different a_1: SEA and IPF.

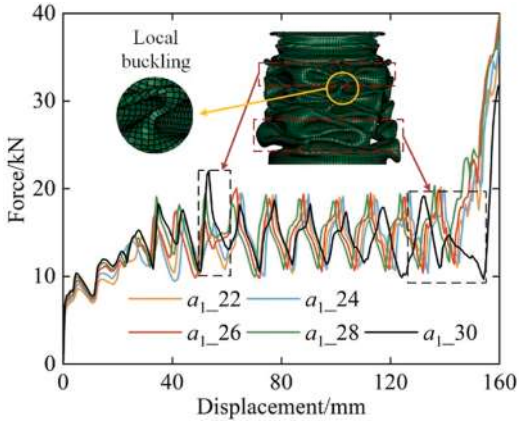

Fig. 16. Force–displacement curves with different a_1.

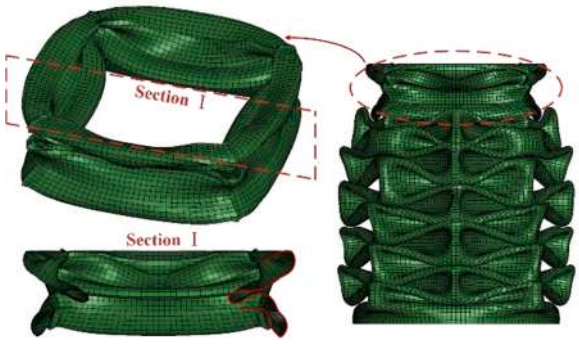

Fig. 17. Deformation mode of θ_150.

Here, we compare the KMS with the pure circular tube (PCT). The PCT has a wall thickness of 0.9 mm, a diameter of 40.5 mm, and a tube length of 200 mm. Results from Table 7 indicate that due to the introduction of the kirigami structure, the KMS exhibits a significant peak clipping. Specifically, T2 has an IPF of 3.839 kN, which is 88.381% lower than that of PCT. Additionally, the CFE of KMS is superior to PCT, and the SEA can maintain its original level. It can be observed from the Fig. 25 that PCT exhibits a three-fold accordion mode plastic hinge during collapse, corresponding to three peak responses, and subsequently transitions into a stable diamond mode deformation, which leads to large loads in the initial stage of collision, resulting in a large initial acceleration which is undesirable for the crashworthiness.

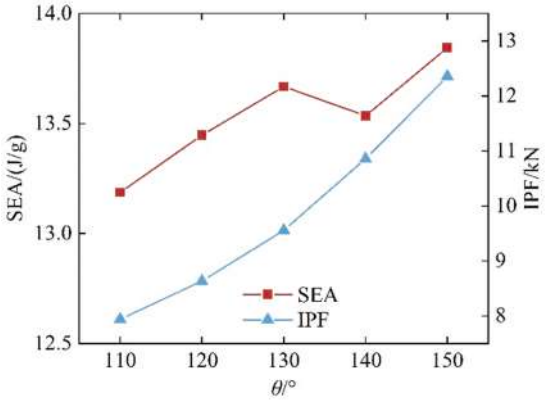

Fig. 18. Crashworthiness indicators with different θ: SEA and IPF.

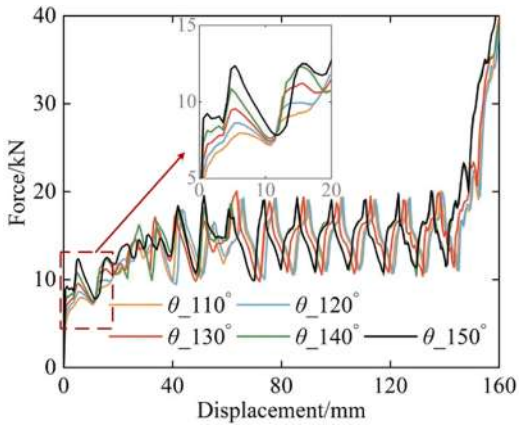

Fig. 19. Force–displacement curves with different θ.

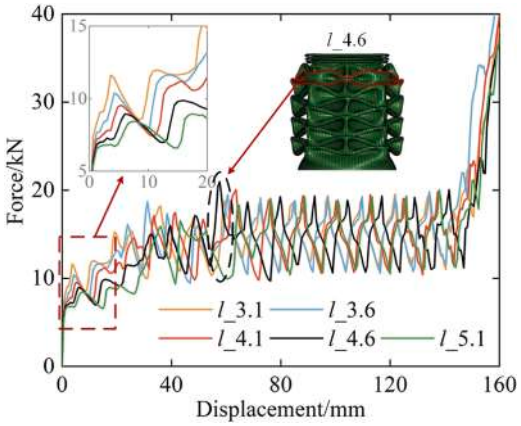

Fig. 20. Force–displacement curves with different l.

However, with the introduction of the kirigami structure, the initial acceleration during collision is reduced, allowing the load to gradually and steadily rise, and the crashworthiness of the EA structure is effectively improved. In summary, by adjusting the thickness gradient distribution, KMS can maintain a high energy absorption while effectively reducing the IPF, thereby improving the structural crashworthiness.

4.3. Multi-stage energy absorption response

In order to approach a smooth and gradual rise followed by a stable plateau in the force–displacement response, the target curve can be

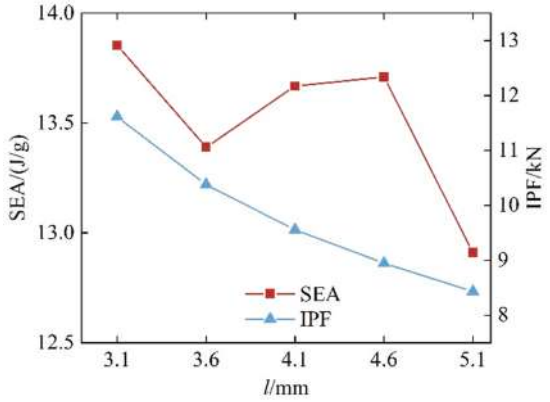

Fig. 21. Crashworthiness indicators with different *l*: SEA and IPF.

Table 6
Thickness of structures with different thickness distributions.

NO.	t_1 (mm)	t_2 (mm)	t_3 (mm)
PCT	/	/	0.9
T1	0.5	0.8	1.1
T2	0.5625	0.8	1.0375
T3	0.625	0.8	0.975
T4	0.6875	0.8	0.9125
T5	0.75	0.8	0.85

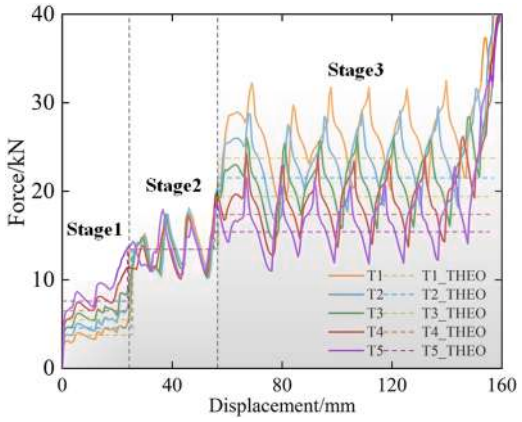

Fig. 22. Force–displacement curves with different thickness gradient.

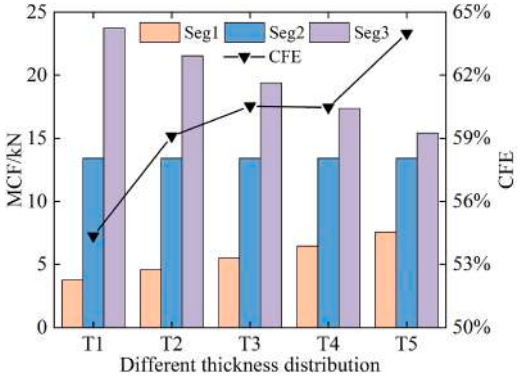

Fig. 23. Crashworthiness indicators with different thickness gradient: MCF and CFE.

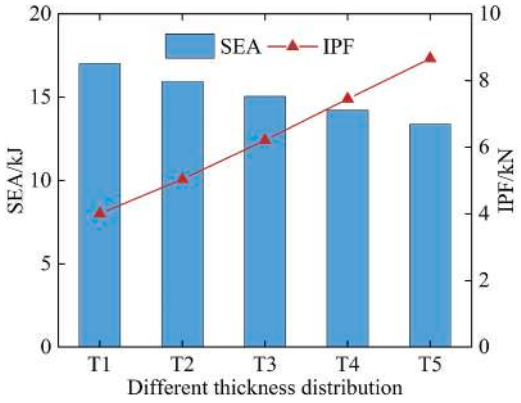

Fig. 24. Crashworthiness indicators with different thickness gradient: SEA and IPF.

Table 7
PCT and T2: structural crashworthiness indicators.

NO.	EA/J	*m*/kg	IPF/kN	SEA/(kJ/kg)	CFE/(%)
PCT	2884.188	0.180	33.042	16.023	57.96
T2	2868.337	0.180	3.839	15.940	59.106

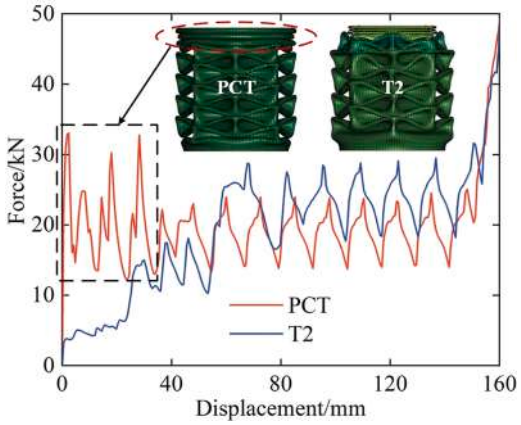

Fig. 25. Force–displacement curves of T2 and PCT.

Table 8
Structural parameters of KMS with a five-stage response.

NO.	Segment	a_1/mm	t_1/mm	*l*/mm	*θ*/°	*N*
Kirigami sturctures	Seg 1	26	0.5	5.1	110	2
	Seg 2	26	0.65	4.6	120	2
	Seg 3	26	0.8	4.1	130	2
Transition segment	Seg 4	l_t/mm 22.49		t_2/mm 0.9		
Circular tube	Seg 5	l_{CCT}/mm 130	t_3/mm 1.0		D/mm 40.5	

discretised into multiple segments, then the kirigami structure can be divided into multiple segments. By controlling parameters, segmented structural stiffness can be formed, further achieving a multi-stage energy absorption force–displacement response. Here, we discuss a KMS with five segment structures, where the kirigami structure is divided into three segments. Based on the analyses in Sections 4.1 and 4.2, by controlling the parameters of each segment, the structure exhibits a certain stiffness gradient distribution in the collision direction, as shown in Table 8. It is observed from Fig. 26 that the KMS exhibits a five-stage force–displacement response, and the result from theoretical analysis align well with simulation one. In terms of deformation modes, the

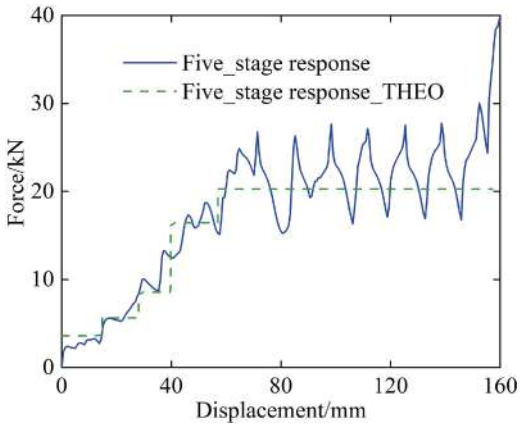

Fig. 26. Five-stage response.

Fig. 27. Deformation mode with a five-stage response.

kirigami structure undergoes sequential deformation, and then the transition segment and the circular tube form a stable diamond mode deformation, as shown in Fig. 27.

It is worth noting that for different collision scenario, the process of the rise of the crushing force is different, and the magnitude of the plateau is also different. The designer can divide the kirigami structure into several segments according to the actual situation, and control the MCF of each segment by adjusting the parameters, so that the force–displacement response of the structure can be more approximate to the rising process of the crushing force of the target curve.

5. Conclusion

The design method proposed in this study approximates the target curve with discrete multi-stage energy absorption response, which can achieve the design of energy-absorbing structures under different collision scenarios. The approximation of the target energy-absorbing curve can be achieved through theoretical analysis guidance and parameter control by using multi-module and multi-stage structures to control the segmental stiffness. Experimental and numerical simulation results demonstrate that the proposed kirigami-based multi-stage energy absorption structure (KMS) achieves progressive segmented dissipation of impact energy, exhibiting excellent crashworthiness. The main conclusions of the study are as follows:

(1) Thanks to the characteristics of stable loading and significant peak clipping in kirigami structures, theoretical analysis of the mean crushing force is derived and employed to guide structural design. By adjusting the geometric parameters of the kirigami structure to control the mean crushing force and crushing stroke, the energy-absorbing structure can approximate the target curve with a multi-stage energy absorption response, thus achieving the design of energy-absorbing structures under different collision scenarios.

(2) Experimental results indicate that the KMS designed for a certain collision scenario exhibits stable deformation under impact loads. Additionally, the kirigami structure effectively induces the circular tube to undergo a stable and ordered diamond mode deformation. Notably, the kirigami structure with a square cross-section demonstrates excellent performance in crashworthiness indicators and force–displacement response, showing a 21.5 % higher SEA compared to that of a circular cross-section.

(3) Numerical examples demonstrate that the kirigami structure dominates the inducing effect on adjacent segments, which may be regulated by design parameters. The deformation mode of the kirigami structure and its induced effect can be effectively controlled by the appropriate parameter design.

(4) Using the proposed design method, the designer can divide the kirigami structure into several segments according to the certain collision scenario, and control the MCF of each segment by adjusting design parameters, in order to enable the force–displacement response of the EA structure to be more approximate to the rising process of the crushing force of the target curve.

From the perspective of structural design, the plateau force and the crushing stroke of kirigami structures are easily controllable, so the designing based on kirigami structures can better achieve discretized multi-stage curves, enabling energy-absorbing structures to cope with requirements of various scenario. Additionally, the study allows for a hybrid design of kirigami structures and circular tubes, and the proposed KMS effectively reduces the initial peak force and acceleration while improving the energy absorption efficiency of the structure. In summary, the design method proposed in this study provides insights into the crashworthiness design of energy-absorbing structures for specific collision scenarios.

CRediT authorship contribution statement

Baofeng Ruan: Writing – original draft, Investigation, Data curation. **Lele Zhang:** Supervision, Funding acquisition, Conceptualization. **Weiyuan Dou:** Writing – review & editing, Methodology, Conceptualization. **Ding Zhang:** Validation. **Sebastian Stichel:** Writing – review & editing.

Declaration of competing interest

The authors declare that they have no known competing financial interests or personal relationships that could have appeared to influence the work reported in this study.

Data availability

Data will be made available on request.

Acknowledgments

This study was supported by the National Natural Science Foundation of China (Grant No. 52202431; Grant No. 52172353) and the Talent Fund of Beijing Jiaotong University (Grant No. 2024XKRC044).

Appendix A

According to the energy principle, ignoring the elastic deformation, the work done by the external force is equal to the plastic energy dissipation during the deformation of the kirigami structure. The energy is dissipated through bending of the stationary plastic hinges and the shape distortion of the panel.

For the kirigami structure with polygonal cross-section, the stationary plastic hinges include horizontal stationary plastic hinges and inclined stationary plastic hinges, which correspond to different bending angles, respectively.

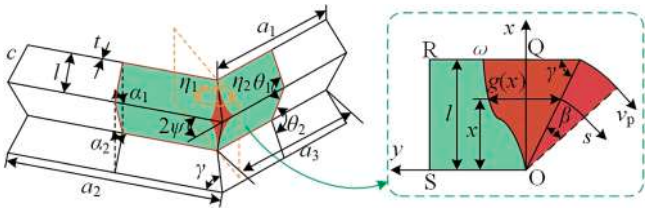

Fig. A1. The parameter of the kirigami structure.

Eq. (A.1) can be utilized to calculate the energy dissipated by bending of the stationary plastic hinges [52]

$$E = M_p \sum l_i \Delta\theta_i \tag{A.1}$$

in which $M_p = \frac{1}{4}\sigma_0 t^2$ is the fully plastic bending moment, l_i is the length of a hinge line i, $\Delta\theta_i$ is the change in bending angle of a hinge line i, and $\sigma_0 = \sqrt{\sigma_y \sigma_u / 1+n}$ is the effective plastic flow stress [62], σ_y is yield strength, σ_u is the ultimate strength and n is the strain hardening exponent, $n = 0.3$.

The energy dissipated along the horizonal stationary plastic hinge lines of length a_1, a_2 and a_3 are respectively calculated as

$$E_{11} = \int_0^{\theta_1} M_p a_1 d\theta_1 = M_p a_1 \theta_1 \tag{A.2}$$

$$E_{12} = \int_0^{\theta_1} M_p a_2 d\theta_1 + \int_0^{\theta_2} M_p a_2 d\theta_2 = M_p a_2 (\theta_1 + \theta_2) \tag{A.3}$$

$$E_{13} = \int_0^{\theta_2} M_p a_3 d\theta_2 = M_p a_3 \theta_2 \tag{A.4}$$

The energy dissipated along the inclined stationary plastic hinge lines of length c_1, and c_2 are respectively calculated as

$$E_{21} = \int_{\eta_1}^{\frac{\pi}{2}} 2M_p c_1 d\eta_1 = M_p c_1 (\pi - 2\eta_1) \tag{A.5}$$

$$E_{22} = \int_{\eta_2}^{\frac{\pi}{2}} 2M_p c_2 d\eta_2 = M_p c_2 (\pi - 2\eta_2) \tag{A.6}$$

The energy is dissipated through the shape distortion in each of four panels, as shown in the red area of Fig. A1, for one of the panels, there is a boundary ω between the stretching deformation region (area red) and the rigid region which is represented by an arbitrary function $g(x)$ [43,62], s is the circumferential curvilinear coordinate from the direction perpendicular to the line OQ, assuming that there is a velocity v that is linear with s, which is in s direction. The velocity v can be expressed as

$$v = \frac{v_P (x/\sin\gamma) s}{c_1 (g(x) + \beta(x/\sin\gamma))}, 0 \le s \le g(x) + \beta(x/\sin\gamma) \tag{A.7}$$

where v_p is the velocity of point P, and $v_P = c_1 \psi \cos\alpha \dot{\alpha}$.

Only the contribution of circumferential strain rate $\dot{\varepsilon}$ to energy dissipation is considered, ignoring the influence of shear strain rate, and $\dot{\varepsilon}$ can be adopted:

$$\dot{\varepsilon} = \frac{v_P (x/\sin\gamma)}{c_1 (g(x) + \beta(x/\sin\gamma))} \tag{A.8}$$

The rate of energy dissipation of stretching in panel can be expressed as

$$\dot{E}_{31} = \int_A \sigma_0 t \dot{\varepsilon} dA = \frac{1}{2}\sigma_0 t c_1^2 \psi \cos\alpha_1 \dot{\alpha}_1 \tag{A.9}$$

where A is the area of the stretching deformation region and $dA = (g(x) + \beta(x/\sin\gamma)) d(x/\sin\gamma)$.

The energy dissipation of stretching can be calculated as

$$E_{31} = \int_{\alpha_1}^{\frac{\pi}{2}} 2M_p \frac{c_1^2}{t} \psi \cos\alpha_1 d\alpha_1 = 2M_p \frac{c_1^2}{t} \psi (1 - \sin\alpha_1) \tag{A.10}$$

Similarly,

$$E_{32} = \int_{\alpha_2}^{\frac{\pi}{2}} 2M_p \frac{c_2^2}{t}\psi \cos\alpha_2 d\alpha_2 = 2M_p \frac{c_2^2}{t}\psi(1-\sin\alpha_2) \tag{A.11}$$

For a kirigami structure of a polygonal cross-section with N modules, the energy dissipation is

$$E_{k\_polygon} = n_{sec}N(E_{11}+E_{12}+E_{13}+E_{21}+E_{22}+2E_{31}+2E_{32}) \tag{A.12}$$

$$E_{k\_polygon} = n_{sec}NM_p\left(a_1\theta_1 + a_2(\theta_1+\theta_2) + a_3\theta_2 + c_1(\pi-2\eta_1) + c_2(\pi-2\eta_2) + 4\frac{c_1^2}{t}\psi(1-\sin\alpha_1) + 4\frac{c_2^2}{t}\psi(1-\sin\alpha_2)\right) \tag{A.13}$$

The energy dissipation of a kirigami structure with a circular cross-section mainly includes the bending of the horizontal stationary plastic hinges and the energy contributed due to the circumferential force.

The length of the horizonal stationary plastic hinge is the circumference of the circular section, and the energy dissipated along the horizonal stationary plastic hinge lines are respectively calculated as

$$E_{41} = \int_0^{\theta_1} M_p \pi d_1 d\theta_1 = M_p \pi d_1 \theta_1 \tag{A.14}$$

$$E_{42} = \int_0^{\theta_1} M_p \pi d_2 d\theta_1 + \int_0^{\theta_2} M_p \pi d_2 d\theta_2 = M_p \pi d_2(\theta_1+\theta_2) \tag{A.15}$$

$$E_{43} = \int_0^{\theta_2} M_p \pi d_3 d\theta_2 = M_p \pi d_3 \theta_2 \tag{A.16}$$

The energy contributed due to the circumferential force [55] can be calculated as

$$\dot{E}_{51} = 2\pi\sigma_0 t\left(l_1^2/2 + 2l_1^3\sin\alpha_1/3d_1\right)\cos\alpha_1\dot{\alpha}_1 \tag{A.17}$$

$$\begin{aligned} E_{51} &= \int_{\alpha_1}^{\frac{\pi}{2}} \pi\sigma_0 t l_1^2 \cos\alpha_1 d\alpha_1 + \int_{\alpha_1}^{\frac{\pi}{2}} 4\pi\sigma_0 t l_1^3 \sin\alpha_1\cos\alpha_1/3d_1 d\alpha_1 \\ &= \frac{4M_p\pi l_1^2}{t}(1-\sin\alpha_1) + \frac{4M_p\pi l_1^3}{3d_1 t}(1+\cos 2\alpha_1) \end{aligned} \tag{A.18}$$

Similarly,

$$\begin{aligned} E_{52} &= \int_{\alpha_2}^{\frac{\pi}{2}} \pi\sigma_0 t l_2^2 \cos\alpha_2 d\alpha_2 + \int_{\alpha_2}^{\frac{\pi}{2}} 4\pi\sigma_0 t l_2^3 \sin\alpha_2\cos\alpha_2/3d_2 d\alpha_2 \\ &= \frac{4M_p\pi l_2^2}{t}(1-\sin\alpha_2) + \frac{4M_p\pi l_2^3}{3d_2 t}(1+\cos 2\alpha_2) \end{aligned} \tag{A.19}$$

For a kirigami structure of a circular cross-section with N modules, the energy dissipation is

$$E_{k\_circle} = n_{sec}N(E_{41}+E_{42}+E_{43}+E_{51}+E_{52}) \tag{A.20}$$

$$E_{k\_circle} = n_{sec}NM_p\pi\left(d_1\theta_1 + d_2(\theta_1+\theta_2) + d_3\theta_2 + \frac{4l_1^2}{t}(1-\sin\alpha_1) + \frac{4l_1^3}{3d_1 t}(1+\cos 2\alpha_1) + \frac{4l_2^2}{t}(1-\sin\alpha_2) + \frac{4l_2^3}{3d_2 t}(1+\cos 2\alpha_2)\right) \tag{A.21}$$

References

[1] V. Acanfora, A. Sellitto, A. Russo, M. Zarrelli, A. Riccio, Experimental investigation on 3D printed lightweight sandwich structures for energy absorption aerospace applications, Aerosp. Sci. Technol. 137 (2023) 108276, https://doi.org/10.1016/j.ast.2023.108276.

[2] J. Pan, H. Fang, M.C. Xu, Y.F. Wu, Study on the performance of energy absorption structure of bridge piers against vehicle collision, Thin-Walled Struct. 130 (2018) 85–100, https://doi.org/10.1016/j.tws.2018.05.008.

[3] L. Hou, H. Zhang, Y. Peng, S. Wang, S. Yao, Z. Li, G. Deng, An integrated multi-objective optimization method with application to train crashworthiness design, Struct. Multidiscp. Optim. 63 (2021) 1513–1532, https://doi.org/10.1007/s00158-020-02758-2.

[4] J. Ma, S. Chai, Y. Chen, Geometric design, deformation mode, and energy absorption of patterned thin-walled structures, Mech. Mater. 168 (2022) 104269, https://doi.org/10.1016/j.mechmat.2022.104269.

[5] A. Baroutaji, M. Sajjia, A.-G. Olabi, On the crashworthiness performance of thin-walled energy absorbers: recent advances and future developments, Thin-Walled Struct. 118 (2017) 137–163, https://doi.org/10.1016/j.tws.2017.05.018.

[6] G. Sun, D. Chen, G. Zhu, Q. Li, Lightweight hybrid materials and structures for energy absorption: a state-of-the-art review and outlook, Thin-Walled Struct. 172 (2022) 108760, https://doi.org/10.1016/j.tws.2021.108760.

[7] X. Zhang, H. Zhang, Axial crushing of circular multi-cell columns, Int. J. Impact Eng. 65 (2014) 110–125, https://doi.org/10.1016/j.ijimpeng.2013.12.002.

[8] X. Zhang, H. Zhang, Z. Wen, Axial crushing of tapered circular tubes with graded thickness, Int. J. Mech. Sci. 92 (2015) 12–23, https://doi.org/10.1016/j.ijmecsci.2014.11.022.

[9] N.S. Ha, T.M. Pham, W. Chen, H. Hao, G. Lu, Crashworthiness analysis of bio-inspired fractal tree-like multi-cell circular tubes under axial crushing, Thin-Walled Struct. 169 (2021) 108315, https://doi.org/10.1016/j.tws.2021.108315.

[10] M. Esa, P. Xue, M. Zahran, M. Abdelwahab, M. Khalil, Novel strategy using crash tubes adaptor for damage levels manipulation and total weight reduction, Thin-Walled Struct. 111 (2017) 176–188, https://doi.org/10.1016/j.tws.2016.11.018.

[11] S. Lykakos, P.K. Kostazos, D.E. Manolakos, Quasi-static axial crushing of thin-walled steel tapered tubes with hybrid geometry: experimental and numerical investigation, Int. J. Crashworthiness 27 (2022) 44–58, https://doi.org/10.1080/13588265.2020.1774037.

[12] X. Xiang, S. Zou, N.S. Ha, G. Lu, I. Kong, Energy absorption of bio-inspired multi-layered graded foam-filled structures under axial crushing, Compos. Part B: Eng. 198 (2020) 108216, https://doi.org/10.1016/j.compositesb.2020.108216.

[13] H. Liang, B. Liu, Y. Pu, H. Sun, D. Wang, Crashworthiness analysis of variable thickness CFRP/Al hybrid multi-cell tube, Int. J. Mech. Sci. 266 (2024) 108959, https://doi.org/10.1016/j.ijmecsci.2024.108959.

[14] S.E. Alkhatib, M.S. Matar, F. Tarlochan, O. Laban, A.S. Mohamed, N. Alqwasmi, Deformation modes and crashworthiness energy absorption of sinusoidally corrugated tubes manufactured by direct metal laser sintering, Eng. Struct. 201 (2019) 109838, https://doi.org/10.1016/j.engstruct.2019.109838.

[15] S. Ming, C. Zhou, T. Li, Z. Song, B. Wang, Energy absorption of thin-walled square tubes designed by kirigami approach, Int. J. Mech. Sci. 157–158 (2019) 150–164, https://doi.org/10.1016/j.ijmecsci.2019.04.032.

[16] Z. Feng, S. Xie, W. Ma, K. Jing, H. Wang, Multi-tube energy-absorbing structures with different matching patterns of heights and diaphragm spacings, Alex. Eng. J. 61 (2022) 11111–11127, https://doi.org/10.1016/j.aej.2022.04.044.
[17] J. Song, Y. Chen, G. Lu, Light-weight thin-walled structures with patterned windows under axial crushing, Int. J. Mech. Sci. 66 (2013) 239–248, https://doi.org/10.1016/j.ijmecsci.2012.11.014.
[18] S. Montazeri, M. Elyasi, A. Moradpour, Investigating the energy absorption, SEA and crushing performance of holed and grooved thin-walled tubes under axial loading with different materials, Thin-Walled Struct. 131 (2018) 646–653, https://doi.org/10.1016/j.tws.2018.07.024.
[19] A.S. Mohamed, O. Laban, F. Tarlochan, S.E. Al Khatib, M.S. Matar, E. Mahdi, Experimental analysis of additively manufactured thin-walled heat-treated circular tubes with slits using AlSi10Mg alloy by quasi-static axial crushing test, Thin-Walled Struct. 138 (2019) 404–414, https://doi.org/10.1016/j.tws.2019.02.022.
[20] G. Lu, J.L. Yu, J.J. Zhang, T.X. Yu, Alexander revisited: upper- and lower-bound approaches for axial crushing of a circular tube, Int. J. Mech. Sci. 206 (2021) 106610, https://doi.org/10.1016/j.ijmecsci.2021.106610.
[21] R. Jiang, Z. Gu, T. Zhang, D. Liu, H. Sun, Z. Pan, D. Peng, Energy absorption characteristics of a CFRP-Al hybrid thin-walled circular tube under axial crushing, Aerospace 8 (2021) 279, https://doi.org/10.3390/aerospace8100279.
[22] M.-K. Kazi, F. Eljack, E. Mahdi, Design of composite rectangular tubes for optimum crashworthiness performance via experimental and ANN techniques, Compos. Struct. 279 (2022) 114858, https://doi.org/10.1016/j.compstruct.2021.114858.
[23] W. Liu, J. Lian, S. Münstermann, C. Zeng, X. Fang, Prediction of crack formation in the progressive folding of square tubes during dynamic axial crushing, Int. J. Mech. Sci. 176 (2020) 105534, https://doi.org/10.1016/j.ijmecsci.2020.105534.
[24] J. Zhang, B. Lu, D. Zheng, Z. Li, Axial crushing theory of metal-FRP hybrid square tubes wrapped with antisymmetric angle-ply, Thin-Walled Struct. 137 (2019) 367–376, https://doi.org/10.1016/j.tws.2019.01.005.
[25] A. Praveen Kumar, M. Yadi Reddy, M. Shunmugasundaram, Energy absorption analysis of novel double section triangular tubes subjected to axial impact loading, Mater. Today: Proc. 47 (2021) 5942–5945, https://doi.org/10.1016/j.matpr.2021.04.485.
[26] K. Li, Y. Feng, Y. Gao, H. Zheng, H. Qiu, Crashworthiness optimization design of aluminum alloy thin-walled triangle column based on bioinspired strategy, Materials (Basel) 13 (2020) 666, https://doi.org/10.3390/ma13030666.
[27] T. Tran, A. Baroutaji, Crashworthiness optimal design of multi-cell triangular tubes under axial and oblique impact loading, Eng. Fail. Anal. 93 (2018) 241–256, https://doi.org/10.1016/j.engfailanal.2018.07.003.
[28] M. Zang, Y. Hu, J. Zhang, W. Ye, M. Zhao, Crashworthiness of CFRP/aluminum alloy hybrid tubes under quasi-static axial crushing, J. Mater. Res. Technol. 9 (2020) 7740–7753, https://doi.org/10.1016/j.jmrt.2020.05.046.
[29] L. Zhang, Z. Bai, F. Bai, Crashworthiness design for bio-inspired multi-cell tubes with quadrilateral, hexagonal and octagonal sections, Thin-Walled Struct. 122 (2018) 42–51, https://doi.org/10.1016/j.tws.2017.10.010.
[30] H. Saeidi Googarchin, M. Pasandidehpoor, A. Mahmoodi, M.H. Shojaeefard, Energy absorption analysis for tapered multi-cell tubes improved by foams: theoretical development and numerical simulation, Compos. Struct. 207 (2019) 213–222, https://doi.org/10.1016/j.compstruct.2018.09.032.
[31] X. Zhang, H. Zhang, Energy absorption of multi-cell stub columns under axial compression, Thin-Walled Struct. 68 (2013) 156–163, https://doi.org/10.1016/j.tws.2013.03.014.
[32] P. Wang, F. Yang, H. Fan, G. Lu, Bio-inspired multi-cell tubular structures approaching ideal energy absorption performance, Mater. Des. 225 (2023) 111495, https://doi.org/10.1016/j.matdes.2022.111495.
[33] F. Wu, Y. Chen, S. Zhao, Y. Hong, Z. Zhang, S. Zheng, Mechanical properties and energy absorption of composite bio-inspired multi-cell tubes, Thin-Walled Struct. 184 (2023) 110451, https://doi.org/10.1016/j.tws.2022.110451.
[34] M.S. Zahran, P. Xue, M.S. Esa, M.M. Abdelwahab, A novel tailor-made technique for enhancing the crashworthiness by multi-stage tubular square tubes, Thin-Walled Struct. 122 (2018) 64–82, https://doi.org/10.1016/j.tws.2017.09.031.
[35] Y. Wang, R. Zhang, S. Liu, X. Zhai, X. Zhi, Energy absorption behaviour of an aluminium foam-filled circular-triangular nested tube energy absorber under impact loading, Structures 34 (2021) 95–104, https://doi.org/10.1016/j.istruc.2021.07.065.
[36] C. Ge, Q. Gao, L. Wang, Z. Hong, Theoretical prediction and numerical analysis for axial crushing behaviour of elliptical aluminium foam-filled tube, Thin-Walled Struct. 149 (2020) 106523, https://doi.org/10.1016/j.tws.2019.106523.
[37] G. Li, F. Xu, G. Sun, Q. Li, A comparative study on thin-walled structures with functionally graded thickness (FGT) and tapered tubes withstanding oblique impact loading, Int. J. Impact Eng. 77 (2015) 68–83, https://doi.org/10.1016/j.ijimpeng.2014.11.003.
[38] M. Rogala, J. Gajewski, M. Ferdynus, The effect of geometrical non-linearity on the crashworthiness of thin-walled conical energy-absorbers, Materials (Basel) 13 (2020) 4857, https://doi.org/10.3390/ma13214857.
[39] J. Fu, Q. Liu, Y. Ma, Z. Zhang, A comparative study on energy absorption of flat sides and corner elements in CFRP square tube under axial compression, Thin-Walled Struct. 166 (2021) 108080, https://doi.org/10.1016/j.tws.2021.108080.
[40] S. Bhutada, M.D. Goel, Progressive axial crushing behaviour of Al6061-T6 alloy tubes with geometrical modifications under impact loading, Thin-Walled Struct. 182 (2023) 110240, https://doi.org/10.1016/j.tws.2022.110240.
[41] H. Nikkhah, F. Guo, Y. Chew, J. Bai, J. Song, P. Wang, The effect of different shapes of holes on the crushing characteristics of aluminum square windowed tubes under dynamic axial loading, Thin-Walled Struct. 119 (2017) 412–420, https://doi.org/10.1016/j.tws.2017.06.036.
[42] K. Tian, Y. Zhang, F. Yang, Q. Zhao, H. Fan, Enhancing energy absorption of circular tubes under oblique loads through introducing grooves of non-uniform depths, Int. J. Mech. Sci. 166 (2020) 105239, https://doi.org/10.1016/j.ijmecsci.2019.105239.
[43] J. Song, Y. Zhou, F. Guo, A relationship between progressive collapse and initial buckling for tubular structures under axial loading, Int. J. Mech. Sci. 75 (2013) 200–211, https://doi.org/10.1016/j.ijmecsci.2013.06.016.
[44] A. Eyvazian, T.N. Tran, A.M. Hamouda, Experimental and theoretical studies on axially crushed corrugated metal tubes, Int. J. Non Linear Mech. 101 (2018) 86–94, https://doi.org/10.1016/j.ijnonlinmec.2018.02.009.
[45] H. Zhang, D. Yu, D. Wang, T. Li, Y. Peng, L. Hou, Z. Li, Crashworthiness of nested corrugation square energy-absorbing tubes with circumferentially cosine profile, Mech. Adv. Mater. Struct. (2023) 1–18, https://doi.org/10.6084/m9.figshare.24210528.v1.
[46] C. Zhou, L. Jiang, K. Tian, X. Bi, B. Wang, Origami crash boxes subjected to dynamic oblique loading, J. Appl. Mech. 84 (2017) 091006, https://doi.org/10.1115/1.4037160.
[47] Z. Li, Q. Yang, R. Fang, W. Chen, H. Hao, Crushing performances of Kirigami modified honeycomb structure in three axial directions, Thin-Walled Struct. 160 (2021) 107365, https://doi.org/10.1016/j.tws.2020.107365.
[48] C. Zhou, T. Li, S. Ming, Z. Song, B. Wang, Effects of welding on energy absorption of kirigami cruciform under axial crushing, Thin-Walled Struct. 142 (2019) 297–310, https://doi.org/10.1016/j.tws.2019.04.037.
[49] C.W. Isaac, F. Duddeck, Current trends in additively manufactured (3D printed) energy absorbing structures for crashworthiness application – a review, Virtual Phys. Prototyp. 17 (2022) 1058–1101, https://doi.org/10.1080/17452759.2022.2074698.
[50] K. Lin, D. Gu, K. Hu, J. Yang, H. Wang, L. Yuan, X. Shi, L. Meng, Laser powder bed fusion of bio-inspired honeycomb structures: effect of twist angle on compressive behaviors, Thin-Walled Struct. 159 (2021) 107252, https://doi.org/10.1016/j.tws.2020.107252.
[51] Y. Wu, L. Sun, P. Yang, J. Fang, W. Li, Energy absorption of additively manufactured functionally bi-graded thickness honeycombs subjected to axial loads, Thin-Walled Struct. 164 (2021) 107810, https://doi.org/10.1016/j.tws.2021.107810.
[52] J. Ma, D. Hou, Y. Chen, Z. You, Quasi-static axial crushing of thin-walled tubes with a kite-shape rigid origami pattern: numerical simulation, Thin-Walled Struct. 100 (2016) 38–47, https://doi.org/10.1016/j.tws.2015.11.023.
[53] Z. Li, S. Yao, W. Ma, P. Xu, Q. Che, Energy-absorption characteristics of a circumferentially corrugated square tube with a cosine profile, Thin-Walled Struct. 135 (2019) 385–399, https://doi.org/10.1016/j.tws.2018.11.028.
[54] S.R. Guillow, G. Lu, R.H. Grzebieta, Quasi-static axial compression of thin-walled circular aluminium tubes, Int. J. Mech. Sci. 43 (2001) 2103–2123, https://doi.org/10.1016/S0020-7403(01)00031-5.
[55] W. Abramowicz, N. Jones, Dynamic axial crushing of circular tubes, Int. J. Impact Eng. 2 (1984) 263–281, https://doi.org/10.1016/0734-743X(84)90010-1.
[56] A. Mahmoodi, M.H. Shojaeefard, H. Saeidi Googarchin, Theoretical development and numerical investigation on energy absorption behavior of tapered multi-cell tubes, Thin-Walled Struct. 102 (2016) 98–110, https://doi.org/10.1016/j.tws.2016.01.019.
[57] A. Schwartz, R. Schneor, G. Molcho, M.W. Cohen, Surface detection and modeling of an arbitrary point cloud from 3D sketching, Comput. Aided Des. Appl. 15 (2018) 227–237, https://doi.org/10.1080/16864360.2017.1375673.
[58] E. Liverani, S. Toschi, L. Ceschini, A. Fortunato, Effect of selective laser melting (SLM) process parameters on microstructure and mechanical properties of 316L austenitic stainless steel, J. Mater. Process. Technol. 249 (2017) 255–263, https://doi.org/10.1016/j.jmatprotec.2017.05.042.
[59] Z. Sun, J. Liu, P. Wang, The predictor-corrector algorithm for hourglass control, Comput. Fluids 209 (2020) 104644, https://doi.org/10.1016/j.compfluid.2020.104644.
[60] Y. Liu, B. Yang, S. Xiao, T. Zhu, G. Yang, R. Xiu, Research on the influence of multiple parameters on the responses of a B-type subway train, Chin. J. Mech. Eng. 35 (2022) 1–18, https://doi.org/10.1186/s10033-022-00755-8.
[61] J. Fang, G. Sun, N. Qiu, N.H. Kim, Q. Li, On design optimization for structural crashworthiness and its state of the art, Struct. Multidiscp. Optim. 55 (2017) 1091–1119, https://doi.org/10.1007/s00158-016-1579-y.
[62] R.J. Hayduk, T. Wierzbicki, Extensional collapse modes of structural members, Comput. Struct. 18 (1984) 447–458, https://doi.org/10.1016/0045-7949(84)90065-8.